

Modeling tabular icebergs coupled to an ocean model

A.A. Stern,¹, A. Adcroft¹ and O. Sergienko¹, G. Marques¹, R. Hallberg¹

² **Key Points:**

³

A. A. Stern, Geophysical Fluid Dynamics Laboratory, Princeton University

A. Adcroft, Geophysical Fluid Dynamics Laboratory, Princeton University

O. Sergienko, Geophysical Fluid Dynamics Laboratory, Princeton University

G. Marques, Geophysical Fluid Dynamics Laboratory, Princeton University

R. Hallberg, Geophysical Fluid Dynamics Laboratory, Princeton University

4 Abstract. The calving of giant icebergs from the Antarctic ice shelves
5 accounts for approximately half of Antarctic ice-shelf decay. After calving,
6 these tabular icebergs drift across large distances, altering regional ocean cir-
7 culation, bottom-water formation, sea-ice production and biological primary
8 productivity in the icebergs' vicinity. However, despite their importance, the
9 current generation of numerical models is unable to represent giant tabular
10 icebergs in a physically realistic way. In this study we develop a novel frame-
11 work to model giant tabular icebergs submerged in the ocean. In this frame-
12 work, tabular icebergs are constructed out of Lagrangian elements that drift
13 in the ocean, and are held together by numerical bonds. By breaking these
14 bonds, a tabular iceberg can be made to split into smaller pieces, or to break
15 away from an ice shelf. We describe the Lagrangian tabular-iceberg model
16 and discuss a number of the technical elements involved in its development.
17 We demonstrate the capabilities of the model by modeling a tabular iceberg
18 drifting away an idealized ice shelf.

1. Introduction

The Antarctic ice shelves are characterized by large infrequent calving events where massive pieces of the ice shelves break off, to create giant tabular icebergs. Observational estimates suggest that over the past 30 years approximately half of Antarctic ice-shelf decay is due to iceberg calving, while the other half occurs through ice-shelf melting [Depoorter et al , 2013; Rignot et al , 2013]. Iceberg sizes appear to fit a power law distribution, with the majority of icebergs being small ($L < 1$ km), while the far less numerous giant tabular icebergs ($L > 5$ km) account for more than 90% of the icebergs mass [Tournadre et al , 2016].

After calving, icebergs slowly drift away from their source glaciers, often becoming stuck in sea ice, or grounding along the Antarctic coast [Lichy and Hellmer , 2001; Dowdeswell and Bamber , 2007]. Giant tabular icebergs extend deep into the water column, and have the potential to disrupt ocean circulation patterns for months or even years after calving [Robinson et al , 2012; Stern et al , 2015]. The freshwater flux from iceberg melt impacts ocean hydrography around the iceberg, influencing sea-ice production and bottom-water formation [Arrigo et al , 2002; Robinson et al , 2012; Nicholls et al , 2009]. The long distances traveled by giant icebergs before melting means that their meltwater impact is often felt hundreds of kilometers away from their calving origins [Stern et al , 2016]. Meltwater injection (and the accompanying upwelling) from icebergs can also influence biological productivity by providing nutrients to the surface ocean or changing sea ice conditions [Arrigo et al , 2002; Vernet et al , 2012; Biddle et al , 2015]. The increased productivity associated with free-floating tabular icebergs has been linked with

40 local increases in ocean carbon uptake, potentially large enough to be a significant fraction
41 of the Southern Ocean carbon sequestration [Smith et al , 2007].

42 In recent years, there has been an increased interest in iceberg drift and decay. This
43 surge of interest has been driven by (i) the need to understand polar freshwater cycles
44 in order to create realistic climate forecasts and sea level projections [Silva et al , 2006;
45 Shepherd and Wingham , 2007; Rignot et al , 2013]; and (ii) the increased use of high-
46 latitudes iceberg-filled waters for shipping lanes and offshore hydrocarbon exploration in
47 the Arctic [Pizzolato et al , 2012; Unger , 2014; Henderson and Loe , 2016]. The increased
48 interest in icebergs has led to the development of numerical models of iceberg drift and
49 decay [Mountain , 1980; Bigg et al , 1997; Gladstone et al , 2001; Kubat et al , 2005], some
50 of which have been included in global General Circulation Models [Martin and Adcroft ,
51 2010; Marsh et al , 2015]. These iceberg drift models treat icebergs as Lagrangian point
52 particles, which are advected by the flow, and melt according to certain parameterizations
53 for icebergs melt. Since icebergs are treated as point particles, iceberg drift models are
54 mostly suitable for modeling icebergs smaller than an ocean grid cell. Consequently, these
55 models have mostly been used to represent icebergs smaller than 3.5km on a global scale
56 [Jongma et al , 2009; Martin and Adcroft , 2010; Marsh et al , 2015].

57 Point-particle iceberg drift models are less suitable for modeling larger tabular icebergs,
58 where the size and structure of the iceberg may be an important feature in determining
59 their drift and decay [Stern et al , 2016]. They also are not suitable for studying the
60 local effects that icebergs have on the surrounding ocean, or the small scale processes that
61 influence iceberg melt and decay [Wagner et al , 2014; Stern et al , 2015]. For this reason,
62 tabular icebergs ($L > 5\text{km}$) are currently not represented in the iceberg drift models used

in climate models, even though observations suggest that tabular icebergs account for the vast majority of the total Southern Hemisphere iceberg mass [Tournadre et al , 2016].

The goal of this study is to develop a new iceberg model where tabular icebergs are explicitly resolved. In this model, icebergs are no longer treated as point particles that interact with the ocean at a single location, but rather icebergs are given structure, so that they interact with the ocean across multiple ocean grid cells and depress the ocean surface over a wide area. To do this, we create tabular icebergs out of many Lagrangian elements with finite extent which are ‘bonded’ together by numerical bonds. The numerical bonds hold the ice elements together and allow a collection of elements to move as a unit. By manually breaking these bonds, we can simulate iceberg calving, allowing us to study the ocean response to giant iceberg detaching from an ice shelf (e.g.: Figure 2 and 3) or the fracturing of a large iceberg into smaller pieces.

The discrete element model (DEM) developed in this study is referred to at the Lagrangian Tabular Iceberg Model (LTIM). Section 2 gives a description of many of the key aspects of the LTIM. Since this model is a new approach to modeling icebergs, we present many of the technical elements involved in constructing the model. In section 3 and 4, we demonstrate the capabilities of the model by simulating a tabular iceberg detaching from an idealized ice shelf.

2. Model description

The LTIM is a Lagrangian particle-based model (or DEM model) in that the objects of the model are Lagrangian elements. Each element represents a mass of ice that is floating in the ocean, and has a position, velocity, mass, and a set of dimensions, which can evolve in time. The motion of each element is determined by a momentum equation which is

solved in the (Lagrangian) reference frame of the element. The elements are forced by oceanic and atmospheric forces, which are provided by the user, or are determined by coupling the LTIM to an ocean/atmosphere model. The elements also interact with one another and can be bonded together to form larger structures. The angular momentum of the elements is not modeled explicitly; instead rotational motion of larger structures emerge as a consequence of bond orientation and collective motion. In different contexts, the LTIM elements can be thought to represent individual icebergs, sea ice flows, or, when the elements are bonded together, they can represent larger structures such as tabular icebergs or ice shelves.

The LTIM model is developed on the code base of an existing iceberg drift model [Martin and Adcroft , 2010; Stern et al , 2016]. When run with the correct set of runtime flags, the model runs as a traditional iceberg drift model.

2.1. Equations of motion

The elements drift in the ocean, forced by atmosphere, ocean and sea-ice drag forces, as well as the Coriolis force and a force due to the sea surface slope. When these ice elements move alone (without interactions with other elements), they can be thought of as representing individual (or clusters of) small icebergs, and follow the same equations described in the iceberg drift model of Martin and Adcroft [2010] (based on the equations outlined in Bigg et al [1997] and Gladstone et al [2001]).

In addition to the environmental forces, the elements in the LTIM model experience interactive forces due to the presence of other elements. Two types of interactive forces are included between elements. The first force is a repulsive force which is applied to elements to prevent them from moving too close to one another. This repulsive force

¹⁰⁷ prevents icebergs from piling up on top of one another. The second interactive force is a
¹⁰⁸ force due to numerical ‘bonds’, and is only applied if two elements are labelled as ‘bonded’.
¹⁰⁹ When two elements are bonded, each element feels an attractive force that prevents the
¹¹⁰ elements from moving too far apart from one another. The interactive forces between two
¹¹¹ bonded elements are defined such that in the absence of other forces the elements come
¹¹² to rest adjacent to one another, with no overlap of the iceberg areas.

The momentum equation for each element is given by

$$M \frac{D\vec{u}}{Dt} = \vec{F}_A + \vec{F}_W + \vec{F}_R + \vec{F}_C + \vec{F}_{SS} + \vec{F}_{SI} + \vec{F}_{IA}, \quad (1)$$

¹¹³ where $\frac{D}{Dt}$ is the total (Lagrangian) derivative, M is the mass of the element, \vec{u} is the
¹¹⁴ velocity of the element, and the terms on the right hand side give the forces on the
¹¹⁵ element due to air drag (\vec{F}_A), water drag (\vec{F}_W), sea ice drag (\vec{F}_{SI}), Coriolis force (\vec{F}_C),
¹¹⁶ wave radiation force (\vec{F}_R), sea surface slope (\vec{F}_{SS}), and interactions with other elements
¹¹⁷ (\vec{F}_{IA}). The environmental forces are the same as those presented in Martin and Adcroft
¹¹⁸ [2010], and are provided for completeness in Appendix A. The details of the interactive
¹¹⁹ forces are provided in below.

2.2. Interactive Forces

The interactive force on an element is calculated by adding together the interactions
with all other elements, such that the interactive force on element i , $(\vec{F}_{IA})_i$ is given by:

$$(\vec{F}_{IA})_i = \sum_{j \neq i} (\vec{F}_{IA})_{ij}, \quad (2)$$

¹²⁰ where $(\vec{F}_{IA})_{ij}$ is the force on element i by element j . Both bonded and repulsive interac-
¹²¹ tions are modeled using elastic stresses with frictional damping. The elastic component

₁₂₂ of the force is a function of the distance between the two elements, while the frictional
₁₂₃ damping force depends on the relative velocity of the two elements.

To describe the forces between two elements, we begin by introducing some notation.

Let \vec{x}_i , \vec{x}_j be the positions of elements i and j. The distance between elements i and j is

$$d_{ij} = |\vec{x}_i - \vec{x}_j|. \quad (3)$$

When calculating the interactive forces between elements, the elements are assumed to be circular. We define the interaction diameter of an element by

$$D_i = 2\sqrt{\frac{A_i}{\pi}}, \quad (4)$$

where A_i is the planar surface area of element i. Using this, we define the critical interactive length scale,

$$L_{ij} = \frac{D_i + D_j}{2}, \quad (5)$$

₁₂₄ which governs interactions between elements i and j. Repulsive forces are only applied
₁₂₅ when $d_{i,j} < L_{i,j}$, while for $d_{i,j} > L_{i,j}$ attractive bonded forces are applied when a bond exists
₁₂₆ between element i and j. Bond and repulsive forces are designed such that in the absence
₁₂₇ of other forces, bonded particles will settle in an equilibrium position where elements are
₁₂₈ separated by the critical interaction length scale $L_{i,j}$.

To aid in notation, we define a bond matrix B_{ij} such that $B_{ij} = 1$ if elements i and j are bonded together and $B_{ij} = 0$ otherwise. Using this notation, the interactive force $(\vec{F}_{IA})_{ij}$ on an element i by an element j is given by

$$(\vec{F}_{IA})_{ij} = \begin{cases} (\vec{F}_e)_{ij} + (\vec{F}_d)_{ij} & \text{if } d_{ij} \leq L_{ij} \\ (\vec{F}_e)_{ij} + (\vec{F}_d)_{ij} & \text{if } d_{ij} > L_{ij} \text{ and } B_{ij} = 1 \\ 0 & \text{if } d_{ij} > L_{ij} \text{ and } B_{ij} = 0. \end{cases} \quad (6)$$

$(\vec{F}_e)_{ij}$ and $(\vec{F}_d)_{ij}$ are the elastic and frictional damping components of the interactive force between elements i and j. The elastic force $(\vec{F}_e)_{ij}$ between elements is given by

$$(\vec{F}_e)_{ij} = -\kappa_e \left(d_{i,j} - L_{i,j} \right) T_{i,j} \vec{r}_{ij}, \quad (7)$$

where $\vec{r}_{ij} = \frac{(\vec{x}_i - \vec{x}_j)}{|\vec{x}_i - \vec{x}_j|}$ is the directional unit vector between the position of element i and j, κ_e is the spring constant, and $T_{i,j}$ is the minimum of the thickness of elements i, j.

The interactive forces obey Newton's 3rd Law (i.e.: $(\vec{F}_{IA})_{ij} = -(\vec{F}_{IA})_{ji}$). The minimum thickness, $T_{i,j}$, is preferred to the average thickness, since this means that for two bonded elements a fixed distance apart, the acceleration due to elastic forces is bounded, even when the thickness of one of the elements approaches zero.

The frictional damping force has components that damp both the relative radial velocity and relative transverse velocities of the two elements. If \vec{r}_{ij}^\perp is the direction vector perpendicular to \vec{r}_{ij} , and $P_{\vec{r}_{ij}}$ and $P_{\vec{r}_{ij}^\perp}$ are the projection matrices that project onto \vec{r}_{ij} and \vec{r}_{ij}^\perp respectively, then the frictional damping force is given by

$$(\vec{F}_d)_{ij} = \left(-c_r P_{\vec{r}_{ij}} - c_t P_{\vec{r}_{ij}^\perp} \right) \cdot (\vec{u}_i - \vec{u}_j) \quad (8)$$

Here c_r and c_t are the radial and transverse drag coefficients. For the simulation below, we set $c_r = 2\sqrt{\kappa_e}$ and $c_t = \frac{1}{4}c_r$ so that the radial elastic force is critically damped, and the transverse damping is sub critical. The damping forces are implemented using an implicit time stepping scheme, to avoid stability issues for very small elements (details found in Appendix B).

The effectiveness of the repulsive forces can be seen in Figure 4, which shows an uncoupled (ice only) simulation where ice elements drift westward into a bay, and eventually come to rest with minimal overlap between elements. The effectiveness of the numerical

bonds is demonstrated in Figure 5, where tabular icebergs (constructed from many ice
 elements bonded together) and individual icebergs (unbonded elements) drift together
 towards a convex coast line. When the tabular icebergs arrive at the coast, they bump
 into the coastline and begin to rotate, influencing the paths of the other icebergs. In
 this example we see that modeling large structures using small elements bonded together,
 allows us to achieve large-scale structure and rotational motion, without having to include
 an equation for the angular momentum of the elements (as discussed in Jakobsen [2001]).
 Animations of these uncoupled simulations can be found in the supplementary materials.

2.3. Initializing element geometry and packing

For purposes of packing, we assume that elements have surface areas which are shaped
 as equally-sized regular hexagons (note that the elements are assumed to be circular
 for proposes of interactions, but are assumed to be hexagonal for packing purposes).
 When packing these elements together, the hexagonal elements are initially arranged in
 a staggered lattice, with each element bonded to the adjacent elements (see Figure 6a).
 In this arrangement, each element (away from the edges) is bonded to six other elements.
 The bonds between elements form a pattern of equilateral triangles, which give the larger
 structure rigidity. The circular shape of elements (used for interactions) is inscribed within
 the hexagonal shape used for packing (Figure 6a). The centers of adjacent elements are
 initially separated by a distance $d_{i,j} = L_{i,j} = 2A_p$, where A_p is the length the apothems
 of the hexagons.

Some experiments were also performed using rectangular elements, arranged in a reg-
 ular (non-staggered) lattice. In this case, each element forms four bonds with adjacent
 elements. However, the resultant structures were found to be much less rigid and tended

₁₆₅ to collapse when sufficient forces was applied. For this reason, hexagonal elements are
₁₆₆ used here.

2.4. Ocean-ice and ice-ocean coupling

₁₆₇ The LTIM model is coupled to the ocean model via a two-way synchronous coupling,
₁₆₈ meaning that ocean model fields are passed to the LTIM model and the LTIM model
₁₆₉ fields are passed back to the ocean model at every time step. Passing fields between the
₁₇₀ two models involves interpolating fields between the Eulerian grid of the ocean model and
₁₇₁ aggregating the ‘Lagrangian grid’ of the LTIM model (i.e.: onto the ice elements).

₁₇₂ The coupling from the ocean model to the LTIM model is straight forward: at every
₁₇₃ time step, the ocean mixed layer temperature, salinity, velocity and sea-ice concentration
₁₇₄ are passed from the ocean model to the LTIM model, to be used in the momentum
₁₇₅ and thermodynamic equations of the ice elements. Since tabular icebergs are explicitly
₁₇₆ resolved in the ocean, it is sufficient for each element to interact with ocean mixed layer
₁₇₇ only (i.e.: there is no need to manually embed icebergs into the ocean by integrating
₁₇₈ ocean fields over the icebergs’ thickness, as suggested in Merino et al [2016]). Within the
₁₇₉ LTIM model, the ocean model fields are interpolated onto the Lagrangian grid using a
₁₈₀ bilinear interpolation scheme. The LTIM model is not sensitive to the chosen interpolation
₁₈₁ scheme.

₁₈₂ The coupling from the LTIM to ocean model is more complex. The LTIM model
₁₈₃ influences the ocean by: (i) applying a pressure to the ocean surface, (ii) imposing heat,
₁₈₄ salinity and mass fluxes on the ocean, associated with ice melting, and (iii) affecting the
₁₈₅ upper ocean by applying a no-slip boundary condition and frictional velocity beneath the
₁₈₆ ice. Fields from the LTIM model are aggregated from the Lagrangian grid to the Eulerian

ocean grid before they are passed to the ocean model. Since LTIM applies large pressures to the ocean surface, the ocean model is sensitive to the interpolation scheme used to map the LTIM fields to the ocean grid. Sudden jumps to the ocean surface pressure can trigger tsunamis within the ocean model, making the ocean model unrealistic.

The aggregation of the LTIM fields onto the ocean grid is done in a way that is consistent with the shape of the elements in the LTIM model (see Section 2.3). Fields are ‘spread’ to the ocean model grid by exactly calculating what fraction of an element’s surface area lies in a particular grid box, and dividing the field in proportion to this fraction. For example, consider a hexagonal element in the LTIM model, which is positioned such that it intersects four ocean grid cells (Figure 6b). In this situation, the mass of the element is divided between these four ocean cells in proportion to the overlap area between the hexagonal element and the grid cell (this fraction is shown by the colors in 6b). An advantage of this approach is that there are no jumps in pressure as an element moves from one grid cell to another.

The numerical calculation of the intersection between hexagons and the ocean grid is simplified by dividing the hexagon into 6 equilateral triangles. This method allows for the intersection to be found even when the hexagon is not aligned with the grid.

The field-spreading scheme is coded with the restriction that an element’s area can only intersect a maximum of four ocean grid cells at a time. A consequence of this is that this sets a limit on the maximum size of elements that can be represented using this model, i.e.: the longest horizontal dimension of an ice element must be smaller than the ocean grid spacing. Larger ice structures are constructed by bonding together smaller elements.

2.5. Thermodynamics

209 The ice elements decay according to a number of melt parameterizations. As the ice
210 elements melt, their mass decreases, and the appropriate salt, mass and heat fluxes are
211 passed to the ocean. In this section we described the melt parametrization for bonded,
212 unbonded and partially bonded elements.

213 As mentioned above, ice elements which do not interact with other elements are modeled
214 identically to the point particle icebergs described in Martin and Adcroft [2010]. These
215 elements melt according to three semi-empirical parametrization for melt commonly used
216 in previous iceberg studies [Gladstone et al , 2001; Martin and Adcroft , 2010]. Three
217 types of iceberg melting are used: basal melt, M_b , melt due to wave erosion, M_e and melt
218 due to buoyant convection, M_v . M_e and M_v are applied to the sides of the ice element,
219 while M_b is applied at the ice element base. The details of M_b . M_v and M_e are given in
220 Appendix A.

221 When multiple elements are bonded together to form larger structures, it is no longer
222 appropriate to use the parameterizations for melt developed for individual point-particle
223 icebergs. An element which is completely surrounded by other elements, is meant to
224 represent a piece of ice in the middle of a large structure, and hence will not experience
225 a melt at its sides due to wave erosion or buoyant convection. Also, the iceberg basal
226 melt rate, M_b described above is based on boundary layer theory of flow past a finite
227 plate, and is only appropriate for basal surfaces where the distance from the leading edge
228 is sufficiently small [Eckert , 1950; Weeks and Campbell , 1973]. For an element in the
229 interior of large structures, the distance from the edge of the structure is large, and so
230 using M_b for the basal melt is not appropriate. Instead, the basal melt, M_s is determined

²³¹ using the three equation model for basal melt, which is a typical melting parametrization
²³² beneath used beneath ice shelves [Holland and Jenkins , 1999].

When using both individual elements and bonded elements in the same simulation, we determine which melt rate parameterizations to use based on the amount of bonds that each element has. An element which is in the center of a large structure will form the maximum number of bonds, while unbonded elements form zero bonds. If maximum number of bonds that an element can form (given the shape of the element) is N_{max} , and the number bonds that an element has is N_b , then the side melt and bottom melt for that element are given by

$$M_{side} = \frac{(N_{max} - N_b)}{N_{max}}(M_v + M_e) \quad (9)$$

and

$$M_{bottom} = \frac{(N_{max} - N_b)}{N_{max}}M_b + \frac{N_b}{N_{max}}M_s \quad (10)$$

²³³ respectively. In this way, elements with no bonds, melt like point-particle icebergs, ele-
²³⁴ ments at the center of large structures melt like ice shelves, and elements at the sides of
²³⁵ large structures have a combination of iceberg side and basal melt, and ice-shelf melt.

2.6. Algorithms and computational efficiency

²³⁶ Including interactions between elements leads to an increase in the computational com-
²³⁷ plexity of the model. In this subsection we comment on some of the algorithmic procedures
²³⁸ that have been used to increase the computational efficiency.

2.6.1. Interactions and Bonds

²⁴⁰ At every time step, we calculate the force on each element due to interactions with every
²⁴¹ other element. In principle, this involves order N^2 operations (for N elements). However,

242 since each element only has repulsive interactions with elements that are less than one
243 ocean grid cell away, and each element only has bonded interactions with a small number
244 of other elements, we are able to reduce the complexity of the system.

245 The complexity reduction is achieved by storing the element data in an efficient way
246 that prevents having to search through all element pairs to check if they are close to
247 one another or are bonded with one another. The data storage system works as follows:
248 pointers to the memory structures containing each element are stored in linked list data
249 structures, which allow elements to be added and removed from the lists easily without
250 restructuring the entire list. Instead of using one list for all the elements on a processor (as
251 was done in the original code [Martin and Adcroft , 2010]), we use a separate linked list
252 for each ocean grid cell. When an element moves between ocean grid cells, it is removed
253 from its original list and added to the list corresponding to its new ocean grid cell. Since
254 the area of elements has to be smaller than the area of an ocean grid cell, the critical
255 interaction length scale (equation 5) is less than the length of a grid cell. This means that
256 elements only experience repulsive forces with elements in the same ocean grid cell, or
257 in one of the 8 adjacent cells. Limiting the possible repulsive interactions to elements in
258 these 9 linked lists substantially reduces the computational time needed to calculate the
259 total interactive force.

260 Bonded interactions are handled differently. Each bond is assigned a piece of memory.
261 Each ice element contains a linked list of each of its bonds (typically up to six bonds
262 per element). At each time step, the code traverses the lists of bonded elements, and
263 adds a bonded force corresponding to these bond. The bonded force is only applied if
264 $d_{i,j} > L_{ij}$, to avoid double counting an interaction. Having a list of bonds stored with

265 each element reduces the computational complexity of bonded interactions from order N^2
266 to order N. Handling bonded attractive forces separately to the repulsive and non-bonded
267 forces means that we do not need to check whether two elements are bonded, which further
268 increases the computational efficiency.

269 **2.6.2. Parallelization and halos**

270 The LTIM model runs on multiple processors in parallel (and the same grid as the
271 ocean decomposition). When elements move from an ocean cell on one processor to an
272 ocean cell on a second processor, the memory has to be passed from one processor the
273 next, added and removed to the appropriate lists and the memory has to be allocated
274 and deallocated correctly. Element interactions across the edge of processors are handled
275 using computational halos. A computational halo is a copy of the edge of a one processor
276 which is appended to the edge of a second processor, so that the first processor can ‘see’
277 the second processor during a time step. Before each time step, elements at the edges of
278 each processor are copied onto the halos of adjacent processors so that they can be used in
279 calculating the interactive forces. After each time step, these halos are removed, and the
280 process is repeated. These halo updates are one of the most computationally expensive
281 parts of the LTIM model.

282 Keeping track of pairs of bonded elements that move across a processor edge requires
283 a lot of book keeping since bonds have to be severed and reconnected. Details of how
284 the bonds are broken and reconnected across processor boundaries are provided in Ap-
285 pendix C.

286 **2.6.3. Time stepping**

287 The ice elements in the LTIM model are advected using a semi-implicit velocity Ver-
288 let time-stepping scheme. The velocity Verlet time stepping scheme is commonly used
289 in DEM models in video games because it is computational efficient and has desirable
290 stability properties [Jakobsen , 2001]. This time stepping scheme was preferred to the
291 Runge-Kutta 4, which was used in the iceberg model of Martin and Adcroft [2010] since
292 the Verlet time stepping only requires a calculation of the interactive forces once per time
293 step (while the Runge-Kutta scheme requires the interactive forces to be calculated four
294 times). Since the calculation of the interactive forces is one of the most computationally
295 expensive part of the algorithm, the Verlet scheme leads to a significant increase in the
296 speed of the model. We note that the Verlet scheme used in the LTIM contains a modifi-
297 cation of the original (fully explicit) velocity Verlet time stepping scheme in that damping
298 terms are treated implicitly (which increases the numerical stability). The details of this
299 time stepping scheme are outlined in Appendix B.

3. Experiment Setup

300 The introduction of Lagrangian elements, numerical bonds and interpolation schemes
301 between the Eulerian and Lagrangian grids (discussed in Section 2) means that we now
302 have the tools to model giant tabular icebergs submerged in the ocean. We demonstrate
303 this capability by simulating a tabular iceberg drifting away from an idealized ice shelf.

3.1. Model configuration

304 We initialized our simulation using the experimental setup created for the Marine Ice
305 Ocean Modeling Inter-comparison Project (MISOMIP) [Asay-Davis et al , 2016]. The
306 configuration consists of an idealized ice shelf in a rectangular domain. The domain is

³⁰⁷ $L_x = 80\text{km}$ wide and $L_y = 480\text{km}$ long, and contains an ice shelf which is grounded on
³⁰⁸ the south side of the domain and has an ice front at $y=650\text{ km}$. The ice thickness and
³⁰⁹ bottom topography of this setup are shown in Figure 7a and 7b respectively, with the
³¹⁰ grounding line position drawn in for reference. The configuration is the same as that of
³¹¹ the Ocean0 setup in the MISOMIP, with a few minor changes to the ice-shelf geometry
³¹² (see Appendix D for details).

3.2. Initializing Lagrangian elements:

³¹³ The idealized ice shelf is constructed out of Lagrangian ice elements. Ice elements are
³¹⁴ hexagonal and are arranged in a regular staggered lattice (as discussed in Section 2.3).
³¹⁵ The sides of the gridded hexagons are initialized with length $S = 0.98\text{ km}$. Gaps along the
³¹⁶ boundaries are filled in using smaller elements so that the total ice-shelf area is preserved.
³¹⁷ The initial mass of the ice elements is determined by a preprocessing inversion step, which
³¹⁸ is the inverse of the ‘mass-spreading’ interpolation procedure discussed in Section 2.3. The
³¹⁹ pre-interpolation ice draft (treating elements as point masses) contains large grid artifacts
³²⁰ (Figures 7c). These grid artifacts are much reduced after the mass-spreading interpolation
³²¹ is applied (Figure 7b).

3.3. Ocean model setup

³²² The LTIM model is coupled to the MOM6 ocean model [Hallberg et al , 2013]. The
³²³ ocean model is run using a vertical coordinate system which is a hybrid between a sigma-
³²⁴ level and a z-level coordinate. In particular, model layers bend underneath the ice shelf as
³²⁵ they would in a sigma-coordinate model, but collapse to zero thickness when they intersect
³²⁶ with bottom topography, as they would in a z-level model. The coordinate system was

327 achieved using ALE regridding-remapping scheme [White et al , 2009]. The model uses a
328 horizontal resolution of 2km, and 72 vertical layers. All simulations were repeated using
329 the ocean model configured in isopycnal mode (results were similar and are not presented
330 here).

331 Ocean parameters are as specified in the MISOMIP configuration [Asay-Davis et al ,
332 2016], and are shown in Table 1. The simulation is initially at rest, with horizontally uni-
333 form initial ocean temperature and salinity profiles which vary linearly between specified
334 surface and bottom values: $T_{top} = -1.9^{\circ}\text{C}$, $T_{bottom} = 1.0^{\circ}\text{C}$, $S_{top} = 33.8 \text{ psu}$, $S_{bottom} = 34.7$.
335 The maximum ocean depth is $H_{ocean} = 720 \text{ m}$. A sponge layer is used on the northern
336 boundary, which relaxes back to the initial temperature and salinity with a relaxation
337 time scale of $T_{sponge} = 0.1 \text{ days}$. Melting is set to zero for ocean cells where the ocean
338 column thickness is less than 10m to avoid using more energy to melt ice than is present
339 in the water column.

3.4. Spinup and iceberg calving:

340 The model is spun up for 5 years with all ice elements being held stationary. After
341 spinup, a giant tabular iceberg is ‘broken off’ from the ice shelf, and allowed to drift into
342 the open ocean. This is achieved by allowing all ice elements initially within a 14.4 km
343 radius of the center of the ice front to move freely while the other ice elements continue
344 to be held stationary. Ice elements less than 12 km from the center of the ice front,
345 are bonded together to form a semi-circular tabular iceberg. A ring of elements whose
346 distance, d , from the ice front center obeys $12 \text{ km} \leq d \leq 14.4 \text{ km}$, are allowed to move
347 freely, but have all their bonds removed. Elements in this half annulus represent fragments
348 of the ice shelf which calve into small pieces during a large calving event. Breaking the

³⁴⁹ bonds of these surrounding elements allows the tabular iceberg to move away from the
³⁵⁰ ice-shelf cavity more easily.

³⁵¹ After the spinup period, a wind stress $\vec{\tau} = \langle \tau_x, \tau_y \rangle = \langle 0.05, 0.05 \rangle \frac{N}{m^2}$ is applied to
³⁵² drive the tabular iceberg away from the ice-shelf cavity. Perturbation experiments were
³⁵³ performed using other wind stress values.

4. Model Results

³⁵⁴ During spinup, the injection of buoyant meltwater at the base of the ice shelf drives a
³⁵⁵ clockwise circulation within the domain (not shown). The circulation compares well with
³⁵⁶ an identical static ice-shelf experiment run using an Eulerian ice shelf model [Goldberg
³⁵⁷ et al , 2012] (a detailed comparison of the Lagrangian and Eulerian ice shelf models is
³⁵⁸ presented in a separate study, and is not shown here).

³⁵⁹ Once spinup is complete, the elements near the ice-shelf front are allowed to move
³⁶⁰ freely, and the icebergs begin to drift away from the ice shelf (see animations in the
³⁶¹ supplementary materials). The semi-circular tabular iceberg moves as a cohesive unit due
³⁶² to the presence of the numerical bonds, while the smaller ice fragments quickly disperse
³⁶³ (Figure 2). The tabular iceberg drifts towards the northward east, driven by the wind
³⁶⁴ and steered by the Coriolis force.

³⁶⁵ A warming of the surface waters is observed around the tabular iceberg, with the largest
³⁶⁶ warming occurring at the ice-shelf front and along the tabular iceberg's rounded edge
³⁶⁷ (Figure 3). This surface warming is caused by upwelling of the warmer waters from
³⁶⁸ beneath the ice shelf and iceberg. As the icebergs drifts away from the ice shelf, these
³⁶⁹ warmer waters remain at the surface, mapping of the wake of the iceberg (Figure 3). The
³⁷⁰ signature of upwelling water in the wake of a drifting tabular iceberg bears some similarity

³⁷¹ to satellite observations of streaks of increased ocean color in the wake of tabular iceberg
³⁷² in the Southern Ocean [Duprat et al , 2016], suggesting that the increased productivity
³⁷³ around icebergs may be driven by upwelling water delivering nutrients to the surface.

³⁷⁴ The motion of the tabular iceberg disturbs the ocean surface, which drives ocean veloc-
³⁷⁵ ities through out the water column (Figure 8). The elevated shears around the tabular
³⁷⁶ iceberg lead to increased vertical mixing in the vicinity of the iceberg, which alters the
³⁷⁷ stratification of the water column (Figure 9), heating the upper ocean. The increased
³⁷⁸ ocean velocities and increased surface temperatures cause elevated melt rates at the base
³⁷⁹ of the ice shelf and iceberg (Figure 10). The largest melt rates are observed at the newly
³⁸⁰ calved ice-shelf front and on the rounded side of the iceberg (Figure 10a), where the
³⁸¹ iceberg calving has created steep ice cliffs. These sharp ice fronts allow for large ocean
³⁸² currents (Figure 10c), which drive the elevated melt rates. The elevated melt rates act
³⁸³ to smooth out the ice front over time, making the ice cliff less steep. While this is likely
³⁸⁴ a real phenomena that could be observed in nature, we should be wary of the modeled
³⁸⁵ velocities at the ice cliffs, since large changes in ice thicknesses are often associated with
³⁸⁶ numerical pressure gradient errors which can drive spurious motion.

³⁸⁷ As mentioned above, the direction (and speed) of the iceberg drift is largely determined
³⁸⁸ by the wind speed and direction. Perturbation experiments using different wind stresses
³⁸⁹ show that for sufficiently large winds, the tabular iceberg drifts to the north east when
³⁹⁰ $\tau_x > 0$, and to the north west when $\tau_x < 0$ (not shown). For a purely zonal wind stress
³⁹¹ with $|\tau_x| \leq 0.01 \frac{N}{m^2}$, the iceberg does not move away from the ice shelf. When the wind
³⁹² is purely offshore ($\tau_x = 0.0 \frac{N}{m^2}$), a meridional wind stress $\tau_y \geq 0.05 \frac{N}{m^2}$ is needed to move
³⁹³ the tabular iceberg away from the ice shelf. While this result is partly an artifact of the

394 artificial shape of the calving iceberg, it is also consistent with Bassis and Jacobs [2013]
395 who noted that calving is a two step process consisting of (i) ice-shelf breaking and (ii)
396 iceberg detachment. The results here suggest that strong (cross-shore) winds may be
397 required to drive large tabular icebergs away from their mother glaciers.

398 Finally, we note that the numerical bonds in the LTIM model are needed in order to
399 allow the tabular iceberg to retain its shape. Comparing the iceberg calving simulation
400 with an identical simulation where all numerical bonds have been removed, shows that
401 in the absence of the bonds, the ice elements quickly disperse (Figure 11). In this case,
402 the model behavior is more similar to an ice-shelf disintegration and does not create a
403 cohesive tabular iceberg. By breaking some (but not all) numerical bonds, we can simulate
404 the fracturing of tabular icebergs, allowing tabular icebergs to break into smaller pieces
405 (Figure ???). The breaking of a tabular iceberg increases decay rate of the iceberg by
406 increasing the surface area of ice exposed to the ocean. Splitting the tabular iceberg into
407 smaller fragments also allows the fragments of the iceberg to move more rapidly, and be
408 more strongly influenced by the wind.

5. Summary

409 In this study we present a novel framework for representing tabular icebergs in numerical
410 ocean models. In this framework, giant tabular icebergs are constructed from collections
411 of Lagrangian elements that are held together by numerical bonds. Constructing tabular
412 icebergs out of many independent elements allows the icebergs to interact with the ocean
413 across a wide area (larger than a grid cell), and behave as if they had a finite size and
414 structure. This is in contrast to previous representations of icebergs in numerical models
415 [Jongma et al , 2009; Martin and Adcroft , 2010; Marsh et al , 2015] that represent

icebergs as point particles. Explicitly resolving tabular icebergs in the ocean allows the icebergs to interact with the ocean in a more realistic way, and allows us to study the effect that tabular icebergs have on the ocean circulation. Including numerical bonds between elements allows for the possibility of breaking bonds to simulate iceberg calving and fracture.

The capabilities of the tabular iceberg model were demonstrated by modeling a tabular iceberg drifting away from an idealized ice shelf (also constructed using Lagrangian elements). The results show that explicitly resolving the iceberg in the ocean allowed for a complex interaction between the tabular iceberg and the surrounding ocean. In our setup, the tabular iceberg is driven away from the ice shelf by ocean currents, wind stress, and the Coriolis force. As the iceberg moves through the water, it disturbs the ocean surface, driving barotropic ocean currents. The motion of the iceberg and melt beneath the iceberg drive upwelling along the sides of the iceberg, which entrains ambient water and causes a warming of the surface ocean in the wake of the iceberg. The changing ocean conditions feed back onto the iceberg, affecting its motion and melt rates. The highest melt rates are observed at edge of the iceberg which has the steepest ice cliff. These have the effect of smoothing out the ice edge over time. Simulations without using numerical bonds showed that these bonds are essential for allowing the iceberg to move as a unit. We also demonstrate that by breaking these numerical bonds we can simulate iceberg fracture, which is important process that increases the rate of iceberg decay.

To our knowledge, the model presented in this study is the first model to explicitly resolve drifting tabular icebergs in an ocean model that can be used for climate. A natural extension of this work is to try to include tabular icebergs into a general circulation model

439 (GCM) used for climate projections. However, before this can be done, there are a number
 440 of issues that need to be resolved: firstly, the question of how and when to introduce
 441 tabular icebergs into the ocean needs to be addressed. For GCM's with active ice shelves,
 442 a calving law is needed to decide when to release the tabular iceberg into the ocean. The
 443 question of what calving law to use is a topic of ongoing research [Benn et all , 2007; Alley
 444 et al , 2008; Levermann et al , 2012; Bassis and Jacobs , 2013] and is still unresolved. One
 445 potential way to temporarily bypass this problem would be to run hindcast simulations
 446 using historically observed calving events. A related issue is the question of how and
 447 when to break the bonds within the freely floating icebergs to simulation iceberg breakup.
 448 Without a rule for iceberg breakup, the tabular icebergs would likely drift to unrealistically
 449 low latitudes. Finally, further work is needed to understand (and model) the interactions
 450 between tabular icebergs and sea ice, and to parametrize the effects of iceberg grounding,
 451 as these interactions play a large role in dictating the trajectories of tabular icebergs.
 452 None-the-less, the technical framework described in this article is potentially a using step
 453 towards including tabular icebergs in global GCM's, and hence a step towards making
 454 more accurate projections of future sea level.

6. Appendix A

6.1. Environmental forces on ice elements

The non-interactive forces on an ice element are as described in [Martin and Adcroft ,
 2010], and are repeated here for completeness. The forces on an element due to air (a),
 ocean (o) and sea ice (si) drag are given by

$$(\vec{F}_a) = \rho_a(0.5c_{a,v}WF + c_{a,h}LW)|\vec{u}_a - \vec{u}|(\vec{u}_a - \vec{u}), \quad (11)$$

$$(\vec{F}_o) = \rho_o(0.5c_{o,v}W(D - T_{si})F + c_{o,h}LW)|\vec{u}_o - \vec{u}|(\vec{u}_o - \vec{u}), \quad (12)$$

$$(\vec{F}_{si}) = \rho_{si}(0.5c_{si,v}WT_{si}F + c_{si,h}LW)|\vec{u}_{si} - \vec{u}|(\vec{u}_{si} - \vec{u}). \quad (13)$$

Here ρ_a , ρ_o , ρ_{si} , are the density of air, ocean and sea ice, respectively. $c_{a,v}$, $c_{o,v}$ and $c_{si,v}$ are the vertical drag coefficients with air, ocean and sea ice, while $c_{a,h}$, $c_{o,h}$ and $c_{si,h}$ are the respective horizontal drag coefficients. \vec{u}_a , \vec{u}_o , \vec{u}_{si} , are the velocities air, ocean and sea ice, respectively. L, W, T, F and D are the length, width, thickness, freeboard and draft of the ice element. The element thickness is related to the draft and freeboard by $T = F + D$ and $D = \frac{\rho}{\rho_o}T$, where ρ is the ice element density. T_{si} is the sea ice thickness.

The wave radiation force (\vec{F}_R) is given by

$$\vec{F}_R = \frac{1}{2}\rho_o c_r g a \min(a, F) 2 \frac{WL}{W + L} \frac{\vec{v}_a}{|\vec{v}_a|} \quad (14)$$

where g is the acceleration due to gravity, a is the wave amplitude empirically related to the wind speed by $a = 0.010125|\vec{v}_a - \vec{v}_o|$, and c_{wd} is the wave drag coefficient defined as

$$c_{wd} = 0.06 \min\left(\max\left[0, \frac{L - L_c}{L_t - L_c}\right], 1\right), \quad (15)$$

where $L_w = 0.32|\vec{v}_a - \vec{v}_o|^2$ is an empirical wave length, $L_c = 0.125L_w$ is the cutoff length, and $L_t = 0.25L_w$ is the upper limit.

The pressure gradient force is approximated as a force due to sea surface slope and given by

$$\vec{F}_{SS} = -Mg\vec{\nabla}\eta \quad (16)$$

where η is the sea surface height.

6.2. Melt rate parametrization

As discussed in Section 2.5, unbounded ice elements in the LTIM model decay according to parameterizations for iceberg decay typically used in iceberg drift models [Martin and

⁴⁶⁶ Adcroft , 2010], while ice elements within larger ice structures have only a basal melt
⁴⁶⁷ given by the three equation model [Holland and Jenkins , 1999] .

For unbonded ice elements, the element thickness decays due to basal melt at a rate M_b , while the length and width of the elements decay as a result of melt due to wave erosion, M_e , and melt due to buoyant convection, M_v . Following Gladstone et al [2001] and Martin and Adcroft [2010], the basal melt rate, wave erosion melt rate, and buoyant convection melt rate are parameterized by

$$M_b = 0.58|\vec{v} - \vec{v}_0|^{0.8} \frac{\tilde{T}_0 - \tilde{T}}{L^{0.2}} \quad (17)$$

$$M_e = \frac{1}{12}S_s \left(1 + \cos [\pi A_i^3] \right) \left(\tilde{T}_0 + 2 \right), \quad (18)$$

$$M_v = \left(7.62 \times 10^{-3} \right) \tilde{T}_0 + \left(1.29 \times 10^{-3} \right) \tilde{T}_0^2. \quad (19)$$

\tilde{T} is the effective iceberg temperature and is set to $\tilde{T} = 4^\circ\text{C}$, \tilde{T}_0 is the temperature at the top of the ocean, A_i is the sea ice area fraction, and S_s is the sea state, which is given by the Beaufort scale

$$S_s = \frac{2}{3}|\vec{u}_a - \vec{u}_o|^{\frac{1}{2}} + \frac{1}{10}|\vec{u}_a - \vec{u}_o| \quad (20)$$

⁴⁶⁸ All three melt rates are in units of meters per day.

⁴⁶⁹ For elements inside larger structures, the melt due to wave erosion and melt due to
⁴⁷⁰ buoyant convection are set to zero, and the basal melt, M_s is given by the standard three
⁴⁷¹ equation model [Holland and Jenkins , 1999].

7. Appendix B

7.1. Modified Verlet Algorithm

⁴⁷² The LTIM model uses a version velocity Verlet time-stepping algorithm, which has been
⁴⁷³ modified to allow part of the forcing to be calculated implicitly. The traditional velocity

Verlet algorithm is commonly used in molecular dynamics, as it is simple to implement, second order accurate and computationally efficient [Swope et al , 1982; Omelyan et al , 2002]. Here we modify the traditional scheme to allow for the drag forces to be modeled implicitly, which prevents large accelerations for element's whose mass approaches zero. To do this, we include both an implicit and explicit acceleration, $a = a^{exp} + a^{imp}$. The explicit acceleration, a^{exp} includes all forcing terms which depend only on the previous time step and the current position, while the implicit acceleration, a^{imp} includes forcing terms which depend on the velocity at the current time step (in particular the drag and Coriolis forces).

Using a time step of Δt , and subscripts to denote the time step (so that $t_{n+1} = t_n + \Delta t$), the modified velocity Verlet scheme can be written as:

$$1) \quad x_{n+1} = x_n + u_n \Delta t + \frac{1}{2} \Delta t^2 \left(a_n^{exp} + a_n^{imp} \right).$$

2) Calculate a_{n+1}^{exp}

$$3) \quad \text{Calculate } a_{n+1}^{imp} \text{ and } u_{n+1} = u_n + \frac{\Delta t}{2} \left(a_n^{exp} + a_{n+1}^{exp} \right) + (\Delta t) a_{n+1}^{imp}$$

This scheme reduces to the traditional velocity Verlet when a^{imp} is set to zero. Note that $a_{n+1}^{exp} = a_{n+1}^{exp}(x_{n+1}, t_n)$ is an explicit function of x_{n+1} and other quantities evaluated at time t_n , while $a_{n+1}^{imp} = a_{n+1}^{imp}(u_{n+1}, x_{n+1}, t_n)$ additionally depends on u_{n+1} , and needs to be solved implicitly. For this reason in step three, a_{n+1}^{imp} and u_{n+1} need to be solved simultaneously, as described in the next subsection.

In equation (1), the forces due to ocean drag, atmospheric drag and sea ice drag are treated implicitly. The force due to sea surface slope and wave radiation are treated explicitly. The Coriolis term is handled using Crank-Nicolson scheme so that half of the effect is implicit and half is explicit. The elastic part of the interactive forces is treated

⁴⁹⁷ explicitly, while the interactive damping is handled semi-implicitly in that the drag force
⁴⁹⁸ on element A by element B depends on the velocities of elements A and B evaluated at
⁴⁹⁹ time t_{n+1} and t_n , respectively.

7.2. Solving for the velocity implicitly

Since this modified scheme contains some forcing terms which are handled implicitly, a_{n+1}^{imp} and u_{n+1} need to be calculated simultaneously. We demonstrate how this is done, using a simplified one-dimensional version of equation (1), neglecting the atmospheric drag, sea ice drag and Coriolis force, so that the only implicitly treated term is the ocean drag. In this demonstration, we use a superscript to denote the ocean drag force, F^o , and ocean velocity, u^o , to avoid confusion with the subscripts indicating time step. We also define an explicit force, F^{exp} , which accounts for all forces not proportional the element velocity. With these simplifications, the implicit and explicit accelerations are

$$a^{exp} = \frac{1}{M}(\vec{F}^{exp}) \quad (21)$$

$$a^{imp} = \frac{1}{M}(F^o) \quad (22)$$

The ocean drag force at time t_{n+1} is modeled (mostly) implicitly as

$$F_{n+1}^o = \tilde{c}^o |u_n^o - u_n| (u_n^o - u_{n+1}), \quad (23)$$

⁵⁰⁰ where \tilde{c}^o is the effective drag coefficient, accounting for the dimensions of the ice element
⁵⁰¹ (see equation 12).

Step 3 of the modified velocity Verlet scheme can be rewritten by introducing an intermediate velocity u^* , which only depends on the velocity and acceleration at time t_n ,

$$u_n^* = u_n + \frac{1}{2}(\Delta t)a_n^{exp}. \quad (24)$$

Using this, the updated velocity (Step 3) can be written

$$u_{n+1} = u_n^* + \frac{\Delta t}{2} a_{n+1}^{exp} + (\Delta t) a_{n+1}^{imp}. \quad (25)$$

Including the forcing terms into this equations gives

$$u_{n+1} = u_n^* + \frac{\Delta t}{2M} (F_{n+1}^{exp}) + \frac{\Delta t}{M} \left(c_w |u_n^o - u_n| (u_n^o - u_{n+1}) \right) \quad (26)$$

Solving for $u(t_{n+1})$ in terms of quantities which only depend on the previous time step gives

$$u_{n+1} = \frac{u_n^* + \frac{\Delta t}{2M} (F_{n+1}^{exp}) + \frac{\Delta t}{M} \left(c_w |u_n^o - u_n| (u_n^o) \right)}{\left(1 + \frac{\Delta t}{M} c_w |u_n^o - u_n| \right)} \quad (27)$$

Once the u_{n+1} has been found, it can be used to calculate the explicit and implicit accelerations, which are required for the next time step.

Finally, we note that the the drag term (equation 23) is not entirely implicit, since the element velocity inside the absolute value is evaluated at time t_n , rather than at time t_{n+1} .

This is done so that we can solve for the updated velocity analytically. One consequence of this is that it can give rise to a small oscillation in the element velocity. This oscillation is addressed by using a predictive corrective scheme: after solving for a first guess of the velocity at time t_{n+1} , this estimate of the velocity is used to update the estimate of the drag force (i.e.: inside the absolute value signs). This updated drag, can now be used to repeat the process described above to find an improved estimate of the velocity. We found that two iterations were sufficient to remove the unwanted oscillation.

The procedure described in this section is easily extended to include more forcing terms and two dimensions (where it involves inverting a 2×2 matrix).

8. Appendix C

515 Connecting bonds across processor boundaries

516 Since the LTIM model is parallelized across multiple processors, it often happens that two
 517 elements on different processes are bonded together. Keeping track of numerical bonds
 518 across processor boundaries requires a lot of book keeping. In this section we describe the
 519 how LTIM model handles bonds across processor boundaries.

520 The basics of the bond bookkeeping work as follows: consider an element A and an
 521 element B that are bonded together. Each element has a copy of the bond (a piece
 522 of memory which describes the bond between the two elements), which is stored with
 523 the element. Let A-B be the bond stored by element A, and B-A be the bond stored
 524 by element B. Bond A-B contains a pointer which points to element B and bond B-A
 525 contains a pointer which points to element A.

526 Consider a situation where element A and B are originally on Processor 1, and then
 527 element B moves to Processor 2. When this occurs, the memory assigned to element B
 528 on processor 1 is removed, and is allocated on Processor 2. This means that the pointer
 529 to element B in bond A-B (stored in element A on Processor 1) is no longer assigned.
 530 Similarly, the pointer to element A in bond B-A (stored in element B on Processor 2) is
 531 no longer assigned. Before the next time step, a halo update occurs, so that there is
 532 a copy of element A in the halo of Processor 2 and a copy of element B in the halo of
 533 Processor 1. After the halo update, the bonds A-B and B-A have to be reconnected on
 534 both Processor 1 and 2. To aid in reconnecting the bonds, a copy of the grid cell number
 535 of element B is stored in the bond A-B and a copy of the grid cell number of element A
 536 is stored in the bond B-A. We refer to this as the ‘most recent address’. Before a bond

537 is moved from one processor to another, the ‘most recent address’ is updated, so that the
538 bond can be reconnected later. To reconnect bond A-B on Processor 1 (for example), we
539 find the most recent address of element B, and search through the list of elements in the
540 grid cell corresponding to the most recent address of element B until element B is found.
541 The pointer to element B in bond A-B is reassigned and the bond is said to be connected.

542 Once all bonds are reconnected, a bond quality control is done where we loop through
543 all bonds and check that they are working properly. To check that a bond is working
544 properly is a four step process. For example, consider the bond A-B stored in element A
545 on Processor 1. To check the quality of this bond, we use the following four steps:

- 546 1. Check that the pointer to element B is assigned on bond A-B (stored on element
547 A).
- 548 2. Check that the corresponding bond B-A exists on element B.
- 549 3. Check that a pointer to element A exists in this bond B-A.
- 550 4. Check that the element A which is being pointed to is the same element A where
551 you started.

552 All four of these tests must pass in order to make sure that the memory is correctly
553 assigned. A useful tool in this process is that each element is assigned a unique number
554 so that elements are easily identified.

9. Appendix D

555 The experiment configuration used to initialize the calving tabular iceberg simulation
556 (in this study) is the same as that of the Ocean0 setup in the MISOMIP, with the following
557 three changes made:

558 1. The ‘calving criteria’ used in the MISOMIP study (which states that all points in
559 the ice shelf with thickness less than 100m are set to zero thickness) has not been used.

560 2. The ice shelf has been thickened on the flanks of the domain, so that the latitude of
561 the grounding line increases away from the center of the ice shelf.

562 3. The ice shelf is configured to be symmetric about its meridional center line ($x = \frac{L_x}{2}$).

563 This was achieved by using the average of the left and right flanks of the ice-shelf thickness.

564 These three changes were made in order to make the circulation beneath the ice shelf
565 easier to interpret.

References

- 566 Asay-Davis, X. S., S. L. Cornford, B. K. Galton-Fenzi, R. M. Gladstone, G. H. Gudmundsson, D. M. Holland, P. R. Holland, and D. F. Martin (2016), Experimental design for
567 three interrelated marine ice sheet and ocean model intercomparison projects: MIS-
568 MIP v. 3 (MISMIP+), ISOMIP v. 2 (ISOMIP+) and MISOMIP v. 1 (MISOMIP1).
569
570 *Geoscientific Model Development* 9, no. 7: 2471.
- 571 Arrigo, K. R., G. L. van Dijken, D. G. Ainley, M. A. Fahnestock, and T. Markus (2002).
572 Ecological impact of a large Antarctic iceberg. *Geophys. Res. Lett.*, 29(7).
- 573 Alley, R. B., H. J. Horgan, I. Joughin, K. M. Cuffey, T. K. Dupont, B. R. Parizek, S.
574 Anandakrishnan, and J. Bassis (2008), A simple law for ice-shelf calving. *Science* 322,
575 no. 5906, 1344-1344.
- 576 Bassis, J. N., and S. Jacobs (2013), Diverse calving patterns linked to glacier geometry.
577 *Nature Geoscience*, 6(10), 833-836.
- 578 Benn, D. I., C. R. Warren, and R. H. Mottram (2007). Calving processes and the dynamics
579 of calving glaciers. *Earth-Science Reviews*, 82(3), 143-179.
- 580 Bigg, G. R., Wadley, M. R., Stevens, D. P., and Johnson, J. A. (1997), Modeling the
581 dynamics and thermodynamics of icebergs. *Cold Regions Science and Technology*, 26(2),
582 113-135.
- 583 Borstad, C. P., A. Khazendar, E. Larour, M. Morlighem, E. Rignot, M. P. Schodlok, and
584 H. Seroussi (2012), A damage mechanics assessment of the Larsen B ice shelf prior to
585 collapse: Toward a physically-based calving law, *Geophys. Res. Lett.*, 39, L18502
- 586 Biddle, L. C., J. Kaiser, K. J. Heywood, A. F. Thompson and A. Jenkins (2015), Ocean
587 glider observations of iceberg-enhanced biological productivity in the northwestern Wed-

- 588 dell Sea, *Geophys. Res. Lett.*, 42, 459465.
- 589 De Rydt, J., and G. H. Gudmundsson (2016), Coupled ice shelf ocean modeling and
590 complex grounding line retreat from a seabed ridge. *J. of Geophys. Res.: Earth Surface*,
591 121(5), 865-880.
- 592 Dunne, J.P., J.G. John,, A.J. Adcroft, S.M. Griffies, R.W. Hallberg, E. Shevliakova,
593 R.J. Stouffer, W. Cooke, K.A. Dunne, M.J Harrison, and J.P. Krasting (2012), GFDL's
594 ESM2 global coupled climate-carbon Earth System Models. Part I: Physical formulation
595 and baseline simulation characteristics. *J. of Climate*, 25(19), 6646-6665.
- 596 Depoorter, M. A., J. L. Bamber, J. A. Griggs, J. T. M. Lenaerts, Stefan RM Ligtenberg,
597 M. R. van den Broek, and G. Moholdt (2013), Calving fluxes and basal melt rates of
598 Antarctic ice shelves. *Nature*, 502(7469), 89-92.
- 599 Determan J., Gerdes R. (1994), Melting and freezing beneath ice shelves: implications
600 from a three-dimensional ocean-circulation model. *Ann. Glaciol.*, 20, 413-419.
- 601 Dowdeswell, J. A., and J. L. Bamber (2007), Keel depths of modern Antarctic icebergs
602 and implications for sea-floor scouring in the geological record. *Marine Geology*, 243(1),
603 120-131.
- 604 Duprat, L. P., G. R. Bigg, and D. J. Wilton (2016), Enhanced Southern Ocean marine
605 productivity due to fertilization by giant icebergs. *Nature Geoscience*.
- 606 Eckert, E. R. G. (1950). Introduction to the Transfer of Heat and Mass. McGraw-Hill.
- 607 Gladstone, R. M., G. R. Bigg, and K. W. Nicholls. (2001), Iceberg trajectory modeling
608 and meltwater injection in the Southern Ocean (19782012). *J. of Geophys. Res.: Oceans*,
609 106(C9), 19903-19915.

- 610 Goldberg, D. N., C. M. Little, O. V. Sergienko, A. Gnanadesikan, R. Hallberg, and M.
611 Oppenheimer (2012), Investigation of land ice?ocean interaction with a fully coupled
612 ice-ocean model: 1. Model description and behavior. *J. of Geophys. Res.: Earth Surface*,
613 117(F2).
- 614 Gladish, C. V., D. M. Holland, P. R. Holland, and S. F. Price (2012), Ice-shelf basal
615 channels in a coupled ice/ocean model. *J. of Glaciol.*, 58(212), 1227-1244.
- 616 Grosfeld K., R. Gerdes, J. Determan (1997), Thermohaline circulation and interaction
617 between ice shelf cavities and the adjacent open ocean. *J. Phys. Oceanogr.*, **102**, C7,
618 15959-15610.
- 619 Grosfeld, K., and H. Sandhger, (2004). The evolution of a coupled ice shelfocean system
620 under different climate states. *Global and Planetary Change*, 42(1), 107-132.
- 621 Hallberg, R., A. Adcroft, J. P. Dunne, J. P., Krasting, R. J., and Stouffer (2013), Sensitiv-
622 ity of twenty-first-century global-mean steric sea level rise to ocean model formulation.
623 *J. of Climate*, 26(9), 2947-2956.
- 624 Holland D. M., Jenkins A. (2001), Adaptation of an isopycnic coordinate ocean model for
625 the study of circulation beneath ice shelves. *Mon. Wea. Rev.*, 129, 1905-1927.
- 626 Holland P. R. and D. L. Feltham (2006), The effects of rotation and ice shelf topography
627 on frazil-laden Ice Shelf Water plumes. *J. Phys. Oceanogr.*, 36, 2312-2327.
- 628 Holland, D. M., and A. Jenkins (1999), Modeling thermodynamic ice-ocean interactions
629 at the base of an ice shelf. *J. of Phys. Oceanogr.* 29.8, 1787-1800.
- 630 Hellmer H.H., Olbers D. J. (1989), A two-dimensional model for the thermohaline circu-
631 lation under an ice shelf. *Antarctic Science*, 1, 325- 336.

- 632 Henderson J., J. S. P. Loe (2016), The Prospects and Challenges for Arctic Oil Develop-
633 ment. *Oil, Gas and Energy Law Journal (OGEL)*, 14 (2)
- 634 Hopkins, M. A. (1996). On the mesoscale interaction of lead ice and floes. *J. of Geophys.*
635 *Res.: Oceans*, 101(C8), 18315-18326.
- 636 Gaskill, H. S., and J. Rochester (1984). A new technique for iceberg drift prediction. *Cold*
637 *Reg. Sci. Technol.*, 8(3), 223-234.
- 638 Jakobsen, T. (2001). Advanced character physics. In *Game Developers Conference*, Vol.
639 3.
- 640 Jenkins, A., P. Dutrieux, S. S. Jacobs, S. D. McPhail, J. R. Perrett, A. T. Webb, and
641 D. White (2010), Observations beneath Pine Island Glacier in West Antarctica and
642 implications for its retreat. *Nature Geo.*, 3(7), 468-472.
- 643 Jacobs, S. S., A. Jenkins, C. F. Giulivi, and P. Dutrieux (2011). Stronger ocean circulation
644 and increased melting under Pine Island Glacier ice shelf. *Nature Geo.*, 4(8), 519-523.
- 645 Jongma, J. I., E. Driesschaert, T. Fichefet, H. Goosse, and H. Renssen (2009), The effect of
646 dynamic-thermodynamic icebergs on the Southern Ocean climate in a three-dimensional
647 model, *Ocean Modell.*, 26, 104113.
- 648 Kubat I., M. Sayed, S. Savage, T. Carrières (2005), An operational model of iceberg drift
649 *Int. J. Off. Polar Eng.*, 15 (2), 125131
- 650 Lewis E.L. and R.G. Perkin (1986), Ice pumps and their rates. *J. of Geophys. Res.*, 91,
651 11756-11762.
- 652 Losch, M. (2008). Modeling ice shelf cavities in a z coordinate ocean general circulation
653 model. *J. of Geophys. Res.: Oceans*, 113(C8).

- 654 Li, B., H. Li, Y. Liu, A. Wang and S. Ji (2014), A modified discrete element model for
655 sea ice dynamics. *Acta Oceanologica Sinica*, 33(1), 56-63.
- 656 Liu, M. B. and G. R. Liu (2010), Smoothed particle hydrodynamics (SPH): an overview
657 and recent developments. *Archives of computational methods in engineering*, 17(1), 25-
658 76.
- 659 Lichéy, C., and H. H. Hellmer (2001). Modeling giant-iceberg drift under the influence of
660 sea ice in the Weddell Sea, Antarctica. *J. of Glaciol.*, 47(158), 452-460.
- 661 Levermann, A., T. Albrecht, R. Winkelmann, M. A. Martin, M. Haseloff, and I. Joughin.
662 (2012), Kinematic first-order calving law implies potential for abrupt ice-shelf retreat.
663 *The Cryosphere*, 6(2), 273-286.
- 664 Mountain, D. G. (1980). On predicting iceberg drift. *Cold Reg. Sci. Technol.*, 1(3-4),
665 273-282.
- 666 Martin, T., and Adcroft, A. (2010), Parameterizing the fresh-water flux from land ice
667 to ocean with interactive icebergs in a coupled climate model. *Ocean Modelling*, 34(3),
668 111-124.
- 669 Marsh, R., V. O. Ivchenko, N. Skliris, S. Alderson, G. R. Bigg, G. Madec, A. T. Blaker
670 Y. Aksenov, B. Sinha, A.C. Coward, and J.L. Sommer (2015), NEMOICB (v1. 0):
671 interactive icebergs in the NEMO ocean model globally configured at eddy-permitting
672 resolution. *Geoscientific Model Development* 8, no. 5 (2015): 1547-1562.
- 673 MacAyeal D.R. (1984), Thermohaline Circulation Below the Ross Ice Shelf: A Conse-
674 quence of Tidally Induced Vertical Mixing and Basal Melting. *J. Geophys. Res.*, 89,
675 597-606

- 676 Merino, N., Le Sommer, J., Durand, G., Jourdain, N. C., Madec, G., Mathiot, P., and
677 Tournadre, J. (2016), Antarctic icebergs melt over the Southern Ocean: climatology
678 and impact on sea ice. *Ocean Modelling*, 104, 99-110.
- 679 Nicholls K.W. (1996), Temperature variability beneath Ronne Ice Shelf, Antarctica, from
680 thermistor cables. *J. Phys. Oceanogr.*, 11, 1199-1210.
- 681 Nicholls KW, Østerhus S, Makinson K (2009), Ice-Ocean processes over the continental
682 shelf of the southern Weddell Sea, Antarctica: a review. *Rev. Geophys.* 47(3).
- 683 Omelyan, I. P., M. I. Mryglod, and R. Folk (2002), Optimized Verlet-like algorithms for
684 molecular dynamics simulations. *Physical Review E*, 65(5), 056706.
- 685 Rignot, E., S. Jacobs, J. Mouginot, and B. Scheuchl (2013), Ice-shelf melting around
686 Antarctica. *Science*, 341, no. 6143 (2013): 266-270.
- 687 Robinson, N. J., M. J. M. Williams, P. J. Barrett, and A. R. Pyne (2010), Observations of
688 flow and ice-ocean interaction beneath the McMurdo Ice Shelf, Antarctica, *J. Geophys.*
689 *Res.*, 115, C03025
- 690 Pizzolato, L., S. E. Howell, C. Derksen, J. Dawson, L. Copland (2014), Changing sea ice
691 conditions and marine transportation activity in Canadian Arctic waters between 1990
692 and 2012, *Climatic Change* 123 (2), 161173.
- 693 Pan, W., A. M. Tartakovsky, and J. J. Monaghan (2013). Smoothed particle hydrody-
694 namics non-Newtonian model for ice-sheet and ice-shelf dynamics. *J. of Comp. Phys.*,
695 242, 828-842.
- 696 Pralong, A., and M. Funk (2005), Dynamic damage model of crevasse opening and appli-
697 cation to glacier calving, *J. Geophys. Res.*, 110, B01309.

- 698 Sergienko, O. V. (2013). Basal channels on ice shelves. *J. of Geophys. Res.: Earth Surface*,
699 118(3), 1342-1355.
- 700 Silva, T. A. M., Bigg, G. R., and Nicholls, K. W. (2006), Contribution of giant icebergs
701 to the Southern Ocean freshwater flux. *J. of Geophys. Res.: Oceans*, 111(C3).
- 702 Smith, K., B. Robison, J. Helly, R. Kaufmann, H. Ruhl, H., T. Shaw, and M. Vernet
703 (2007), Free-drifting icebergs: Hotspots of chemical and biological enrichment in the
704 Weddell Sea, *Science*, 317, 478482.
- 705 Shepherd, A., and D. Wingham (2007). Recent sea-level contributions of the Antarctic
706 and Greenland ice sheets. *Science*, 315(5818), 1529-1532.
- 707 Stern, A. A., D. M. Holland, P. R. Holland, A. Jenkins and J. Sommeria (2014), The effect
708 of geometry on ice shelf ocean cavity ventilation: a laboratory experiment. *Experiments*
709 *in Fluids*, 55(5), 1-19.
- 710 Stern, A.A., Johnson, E., Holland, D.M., Wagner, T.J., Wadhams, P., Bates, R., Abra-
711 hamsen, E.P., Nicholls, K.W., Crawford, A., Gagnon, J. and Tremblay, J.E. (2015),
712 Wind-driven upwelling around grounded tabular icebergs. *J. of Geophys. Res.: Oceans*,
713 120(8), 5820-5835.
- 714 Stern, A. A., A. Adcroft, and O. Sergienko (2016), The effects of Antarctic iceberg calving
715 size distribution in a global climate model. *J. of Geophys. Res.: Oceans*, 121(8), 5773-
716 5788.
- 717 Swope, W. C., H. C. Andersen, P. H. Berens, and K. R. Wilson (1982), A computer
718 simulation method for the calculation of equilibrium constants for the formation of
719 physical clusters of molecules: Application to small water clusters. *The Journal of*
720 *Chemical Physics* 76, no. 1, 637-649.

- 721 Tournadre, J., N. Bouhier, F. Girard-Ardhuin, and F. Rmy (2016), Antarctic icebergs
722 distributions 1992-2014. *J. Geophys Res: Oceans*.
- 723 Turnbull I.D., N. Fournier, M. Stolwijk, T. Fosnaes, D. McGonigal (2015), Operational
724 iceberg drift forecasting in Northwest Greenland, *Cold Reg. Sci. Technol.* 110, 1-18
- 725 Unger, J. D., 2014. Regulating the Arctic Gold Rush: Recommended Regulatory Reforms
726 to Protect Alaska's Arctic Environment from Offshore Oil Drilling Pollution . *Alaska*
727 *L. Rev*, 31
- 728 Vernet, M., et al. (2012), Islands of ice: Influence of free-drifting Antarctic icebergs on
729 pelagic marine ecosystems, *Oceanography*, 25(3), 3839
- 730 Wagner, T. J., Wadhams, P., Bates, R., Elosegui, P., Stern, A., Vella, D., E. P. Abraham-
731 sen, A. Crawford, and Nicholls, K. W. (2014), The footloose mechanism: Iceberg decay
732 from hydrostatic stresses. *Geophys. Res. Lett.*, 41(15), 5522-5529.
- 733 Weeks, W. F., and W. J. Campbell (1973). Icebergs as a fresh-water source: an appraisal.
734 *J. of Glaciol.*, 12(65), 207-233.
- 735 White, L., A. Adcroft, and R. Hallberg (2009), High-order regridding-remapping schemes
736 for continuous isopycnal and generalized coordinates in ocean models. *J. of Comp.*
737 *Phys.*, 228(23), 8665-8692.

738 (a) Hexagonal elements are initialized in a staggered lattice as shown. Adjacent elements
739 are bonded together. The element bonds (plotted in pink) form equilateral triangles
740 which give the larger structure rigidity. The black circles show the circular element shape
741 used in element interactions, and are inscribed inside the hexagonal shape used for mass-
742 spreading. (b) Intersection of a hexagonal element and the ocean grid. The colors indicate
743 the fraction of the hexagon that lies in each grid cell. These fractions are used as weights
744 to spread LTIM properties to the ocean grid (see text for more details).

Parameter	Symbol	Value	Unit
Domain Length	L_x	80	km
Domain Width	L_y	480	km
Horizontal Resolution	Δx	2	km
Number of vertical layers	N_l	72	non-dim
Horizontal Viscosity	ν_H	6.0	$\frac{m^2}{s}$
Diapycnal Viscosity	ν_V	10^{-3}	$\frac{m^2}{s}$
Horizontal Diffusivity	ϵ_H	1.0	$\frac{m^2}{s}$
Diapycnal Diffusivity	ϵ_V	5×10^{-5}	$\frac{m^2}{s}$
Initial Surface Temperature	T_t	-1.9	$^{\circ}C$
Initial Bottom Temperature	T_b	1.0	$^{\circ}C$
Initial Surface Salinity	S_t	33.8	psu
Initial Bottom Salinity	S_b	34.7	psu
Maximum Ocean depth	H_{ocean}	720	m
Relaxation Time of Sponge Layer	T_{sponge}	0.1	days
Time Step for Static Shelf Experiment	dt_{Static}	1000	s
Time Step for Iceberg Calving Experiment	$dt_{Calving}$	10	s

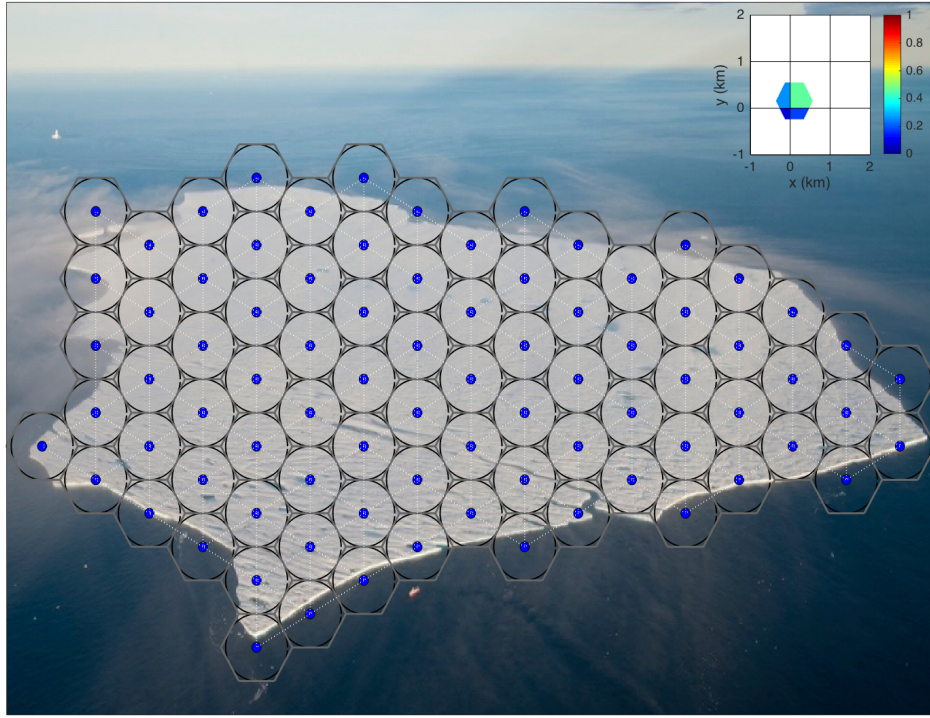


Figure 1. Schematic showing how Lagrangian elements are used when modeling tabular icebergs. Lagrangian elements (blue dots) are initialized in a staggered lattice covering the surface area of the iceberg. For purposes of mass aggregation, the ice elements are assumed to have hexagonal shape (grey hexagons). For purposes of element interactions, the ice elements are assumed to be circular (black circles). Elements are initially bonded to adjacent elements using numerical bonds (dashed white lines). These numerical bonds form equilateral triangles which give the shape rigidity. The inset panel shows a schematic of the intersection of a hexagonal element and the ocean grid. The colors indicate the fraction of the hexagon that lies in each grid cell. These fractions are used as weights to spread LTIM properties to the ocean grid (see text for more details) The background photo in the larger schematic is an areal photograph of iceberg PIIB (Area= 42 km²) taken in Baffin Bay in 2012. The red ship can be identified on the bottom of the photo for scale.

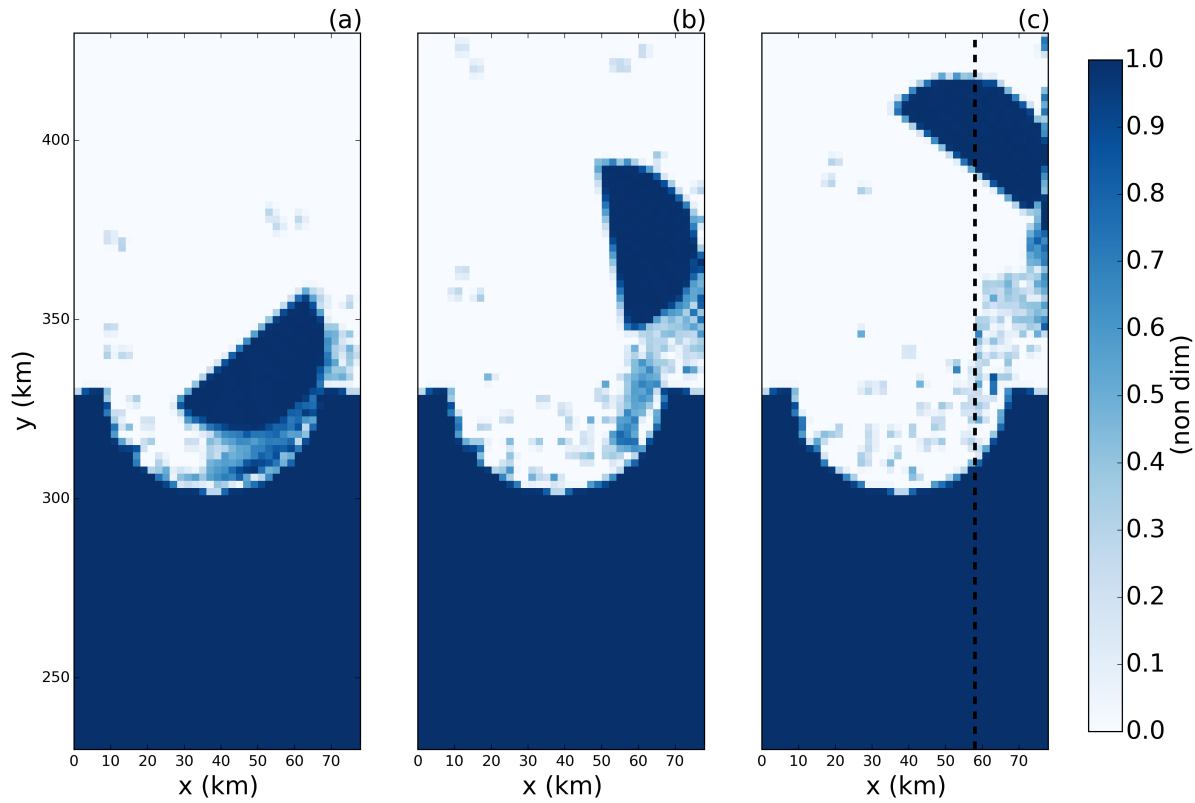


Figure 2. Snapshots of the fraction of ice cover in the LTIM tabular iceberg calving simulation. Snapshots are taken (a) 7, (b) 15, and (c) 30 days after calving. The dashed line in panel (c) shows the location of the vertical transects shown in Figures 8 and 9.

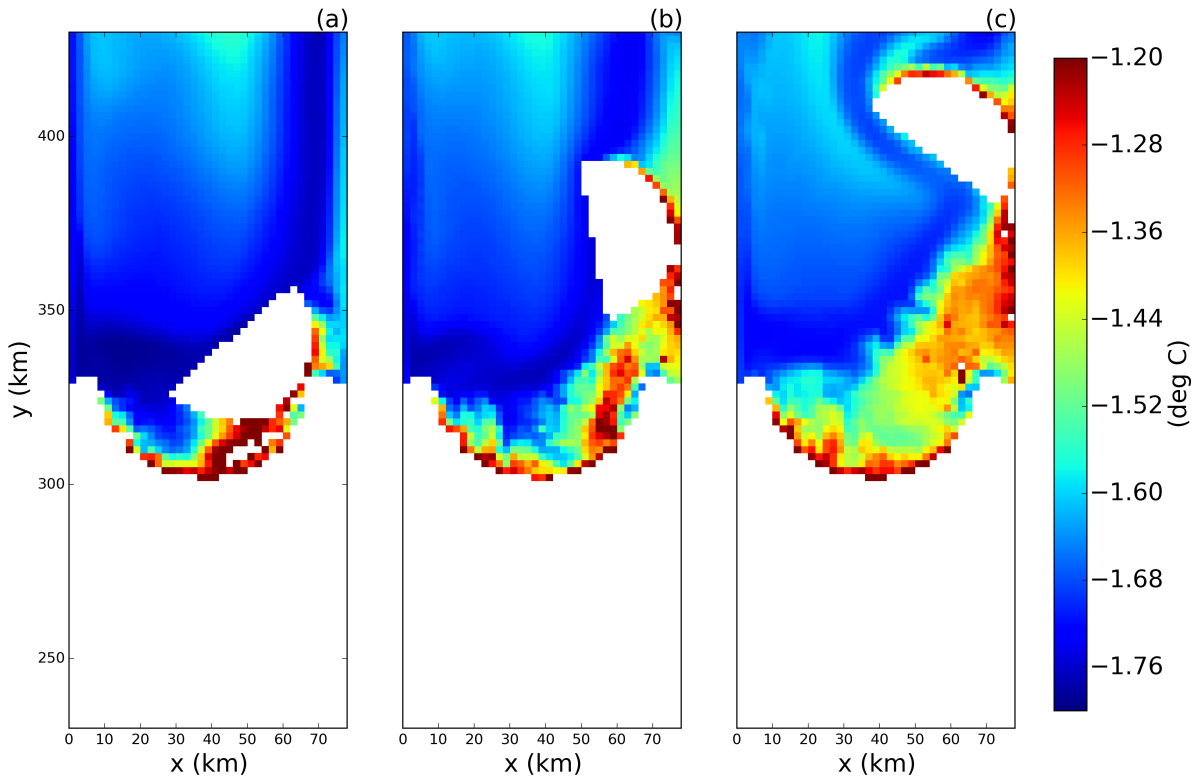


Figure 3. Snapshots of the sea surface temperature in the LTIM tabular iceberg calving simulation. Snapshots are taken (a) 7, (b) 15, and (c) 30 days after calving. Regions with ice area fraction = 1 area plotted in white.

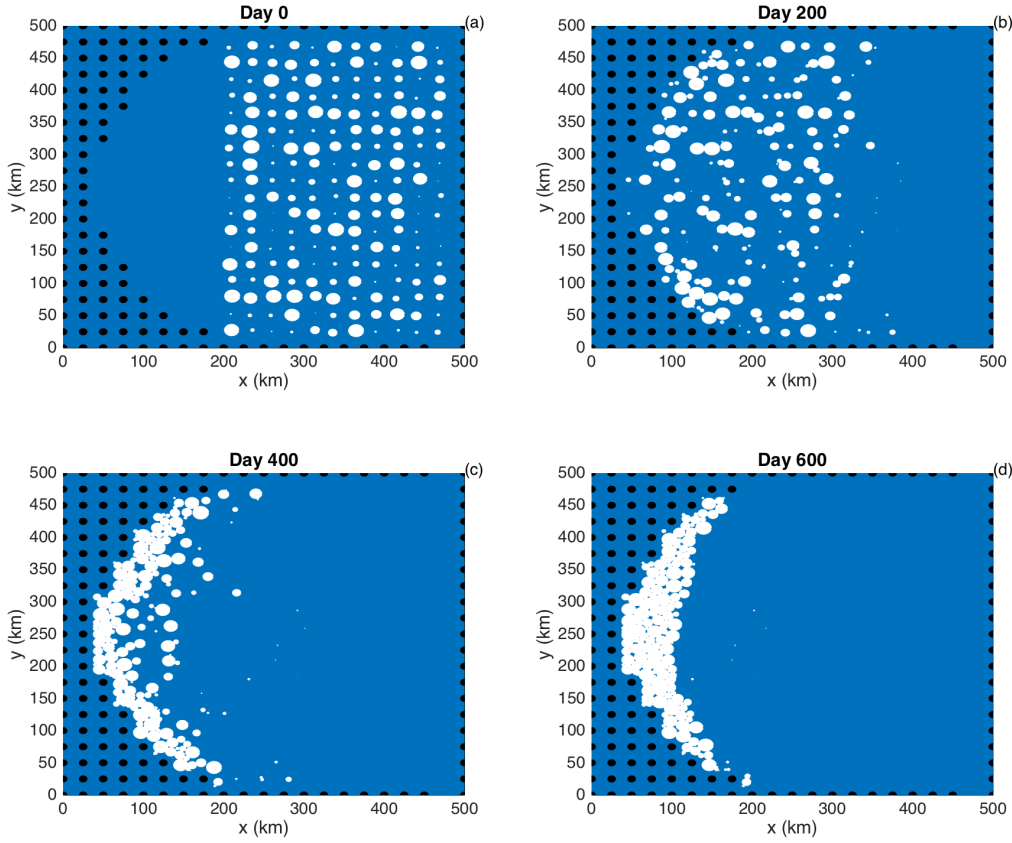


Figure 4. Results of an ice-only LTIM simulation with no bonds between ice elements.

Ice elements are initialized throughout the domain, as shown in panel (a). The elements are forced by an imposed westward ocean current of $u=0.1\text{m/s}$ (no ocean model is used). Forces due to sea surface slope, atmospheric drag, Coriolis and sea ice drag are set to zero. The figure shows snapshots of ice element positions at time (a) $t=0$, (b) 200, (c) 400, (d) 600 days. The size of the dots shows the surface area (and interaction diameter) of each ice element. Land points are shown by black circles.

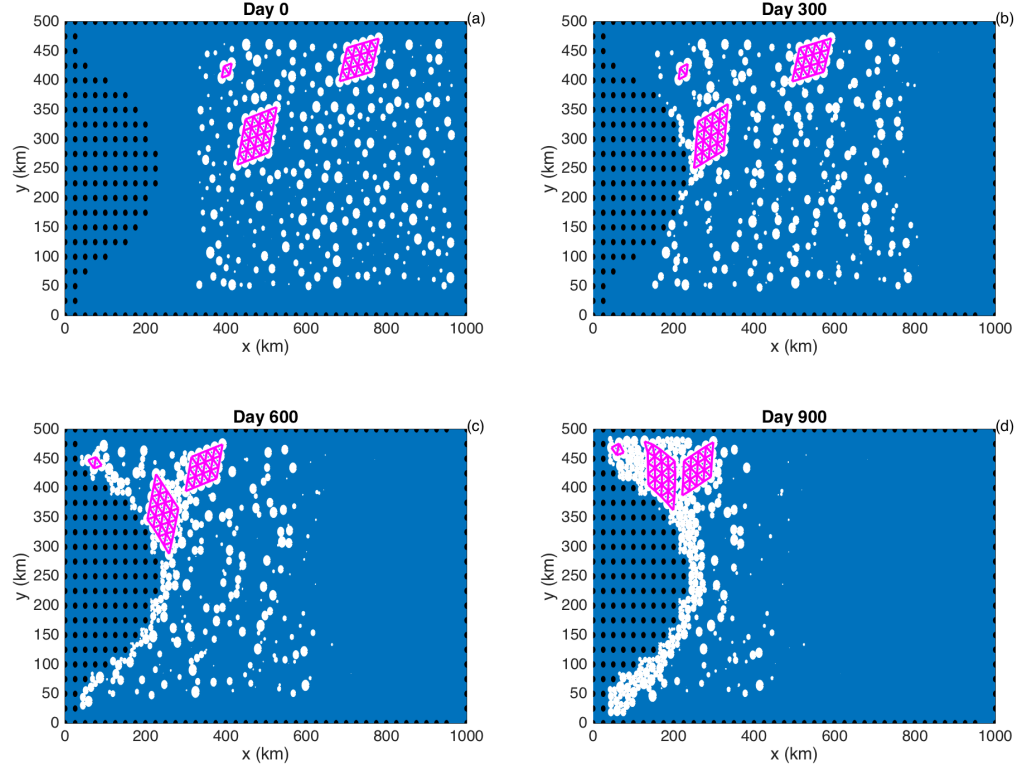


Figure 5. Results of an ice-only LTIM simulation using bonds between elements. Ice elements are initialized throughout the domain, as shown in panel (a). Three tabular icebergs are included, with 25, 16 and 4 elements respectively. The elements are forced by an imposed westward ocean current of $u=0.1\text{m/s}$ (no ocean model is used). Forces due to sea surface slope, atmospheric drag, Coriolis and sea ice drag are set to zero. The figure shows snapshots of ice element positions at time (a) $t=0$, (b) 300, (c) 600, (d) 900 days. The size of the dots shows the surface area (and interaction diameter) of each ice element. Bonds between ice elements are plotted in magenta. Land points are shown by black circles.

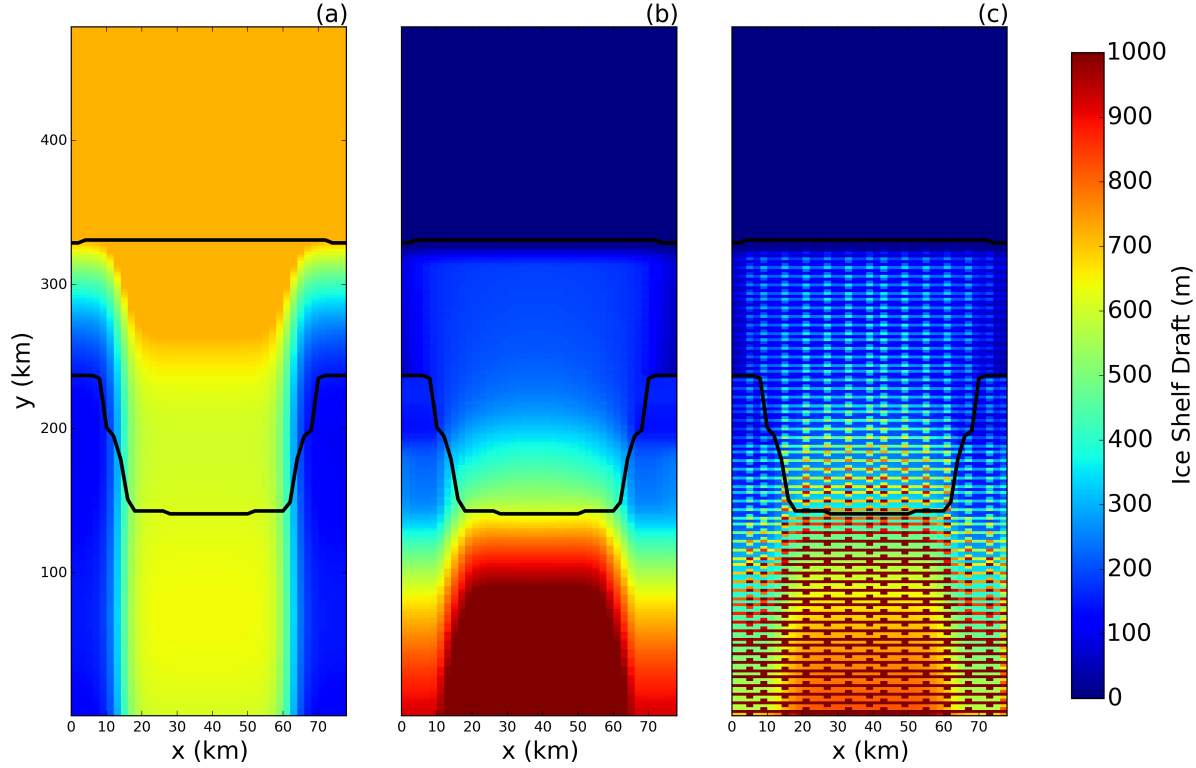


Figure 6. (a) Ocean bottom topography and (b) ice-shelf draft used to initialized the tabular iceberg calving simulation. The ice draft is calculated from the total mass in an ocean grid cell after the mass-spreading interpolation has been applied (as explained in Section 2.3). (c) Initial ice draft that would be calculated if the mass-spreading interpolation were not used (i.e.: elements treated as point masses).

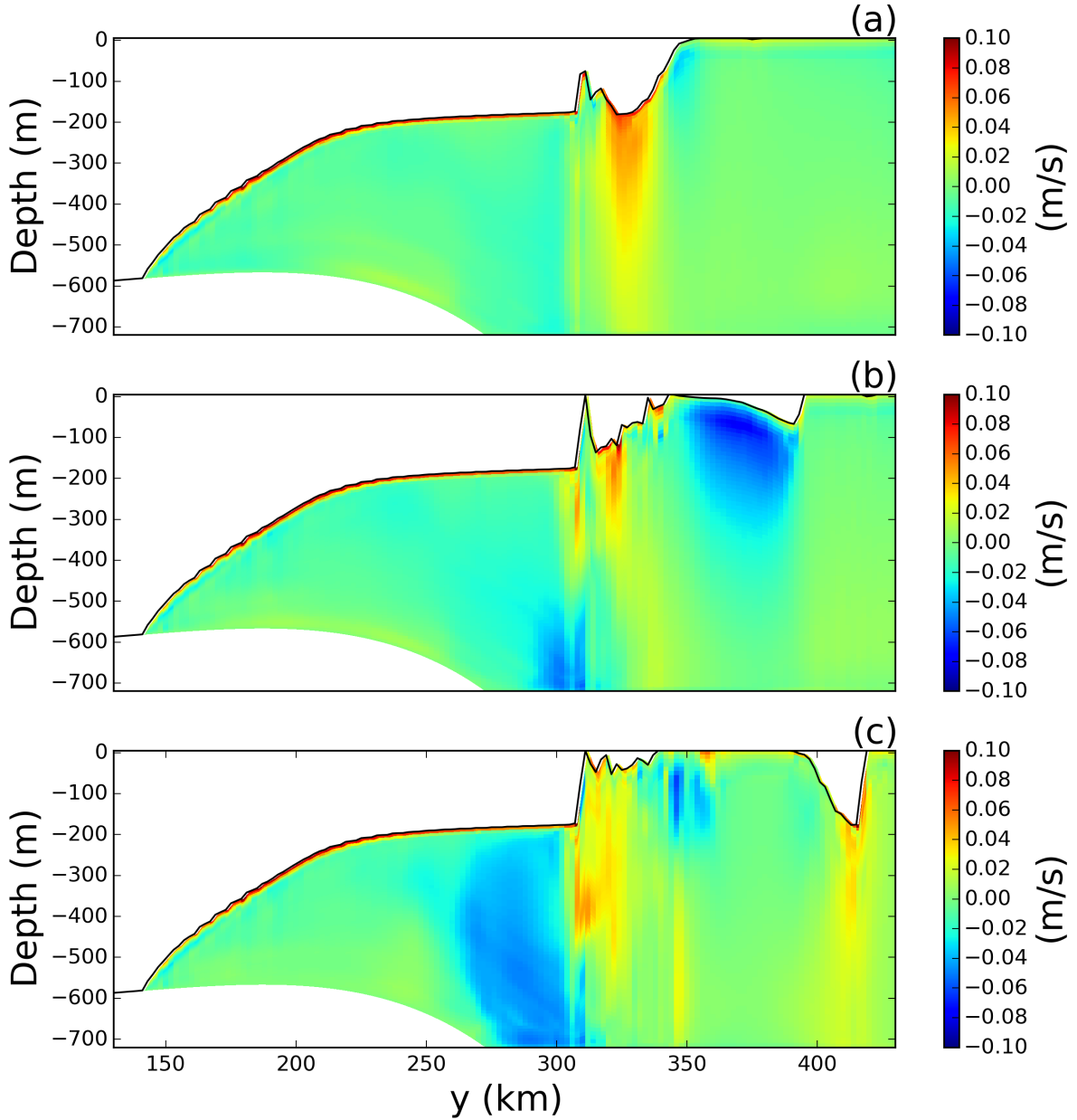


Figure 7. Snapshots of vertical sections of meridional velocity at $x = 58$ km in the LTIM tabular iceberg calving simulation. Snapshots are taken (a) 7, (b) 15, and (c) 30 days after calving. The position of the transects is shown by the dashed line in Figure 2c.

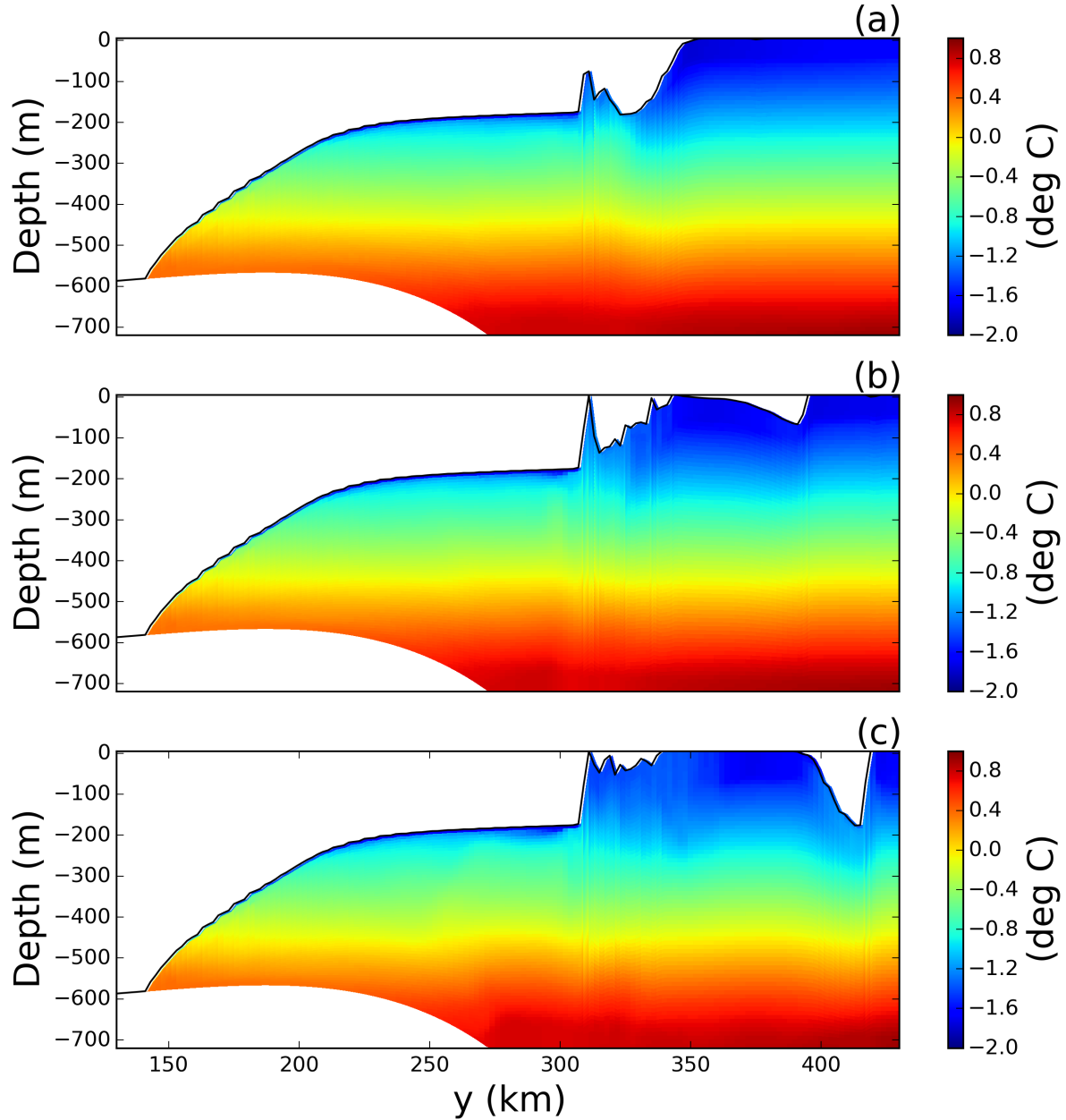


Figure 8. Snapshots of vertical sections of ocean temperature at $x = 58\text{ km}$ in the LTIM tabular iceberg calving experiment. Snapshots are taken (a) 7, (b) 15, and (c) 30 days after calving. The position of the vertical transects is shown by the dashed lines in Figure 2c.

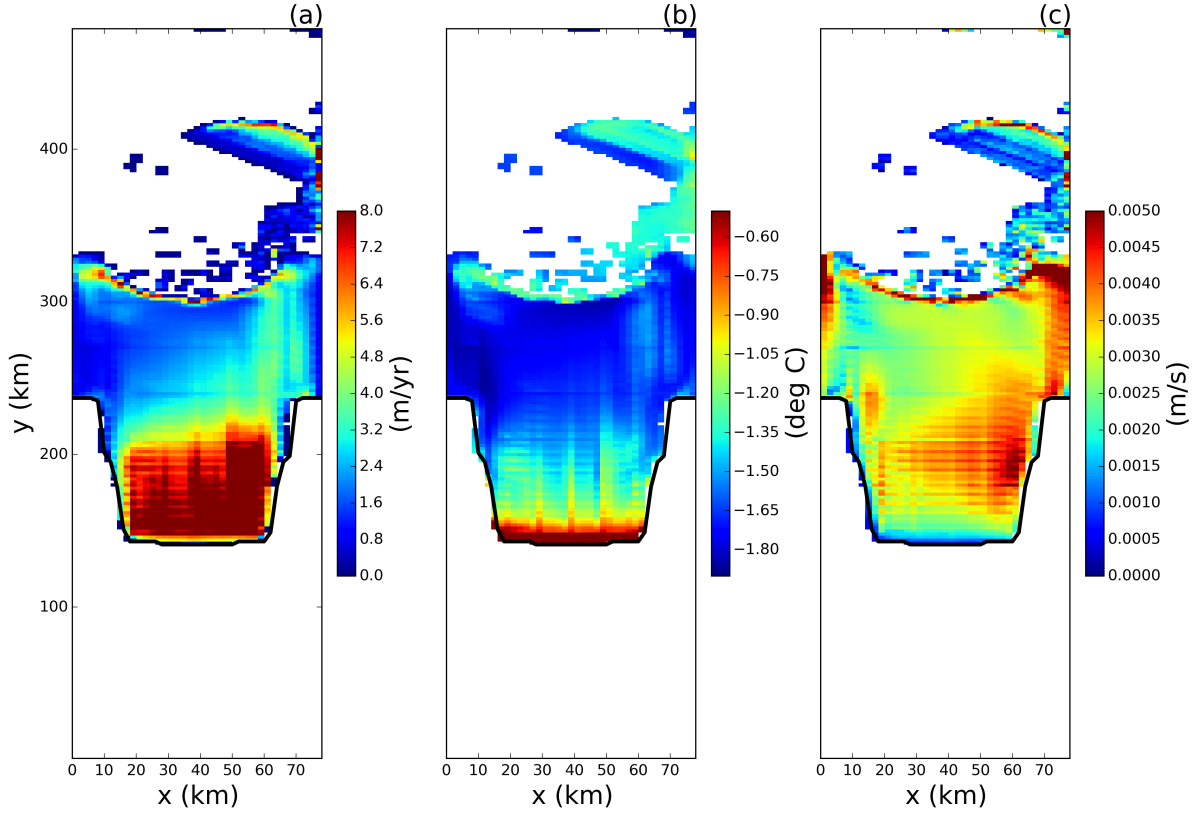


Figure 9. Results of the tabular iceberg calving simulation 30 days after the iceberg calves. The three panels show snapshots of the (a) melt rate, (b) top-of-ocean temperature and (c) u^* at the base of the ice shelf. Fields are only shown in regions where the ice area fraction is ≥ 0.8 .

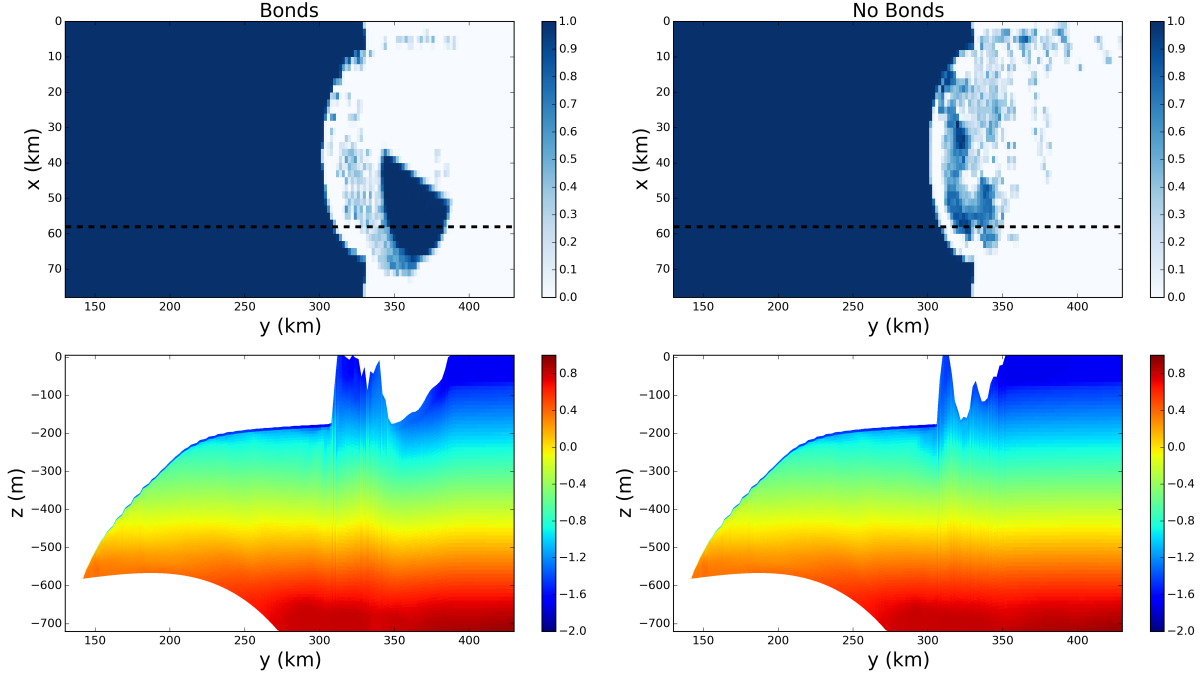


Figure 10. Results from the tabular iceberg calving experiment with and without iceberg bonds. The top row shows the fractional ice cover for the simulations (a) with and (b) without numerical bonds. The bottom row shows the corresponding vertical temperature section at $x = 58\text{km}$ for the simulation (c) with and (d) without bonds. The location of the vertical transects in panels (c) and (d) are shown by the dashed lines in panels (a) and (b), respectively. All snapshots are taken at time $t = 30$ days. The simulations use wind stress $\vec{\tau} = <0.0, 0.05>$.

10. Extra Figure:

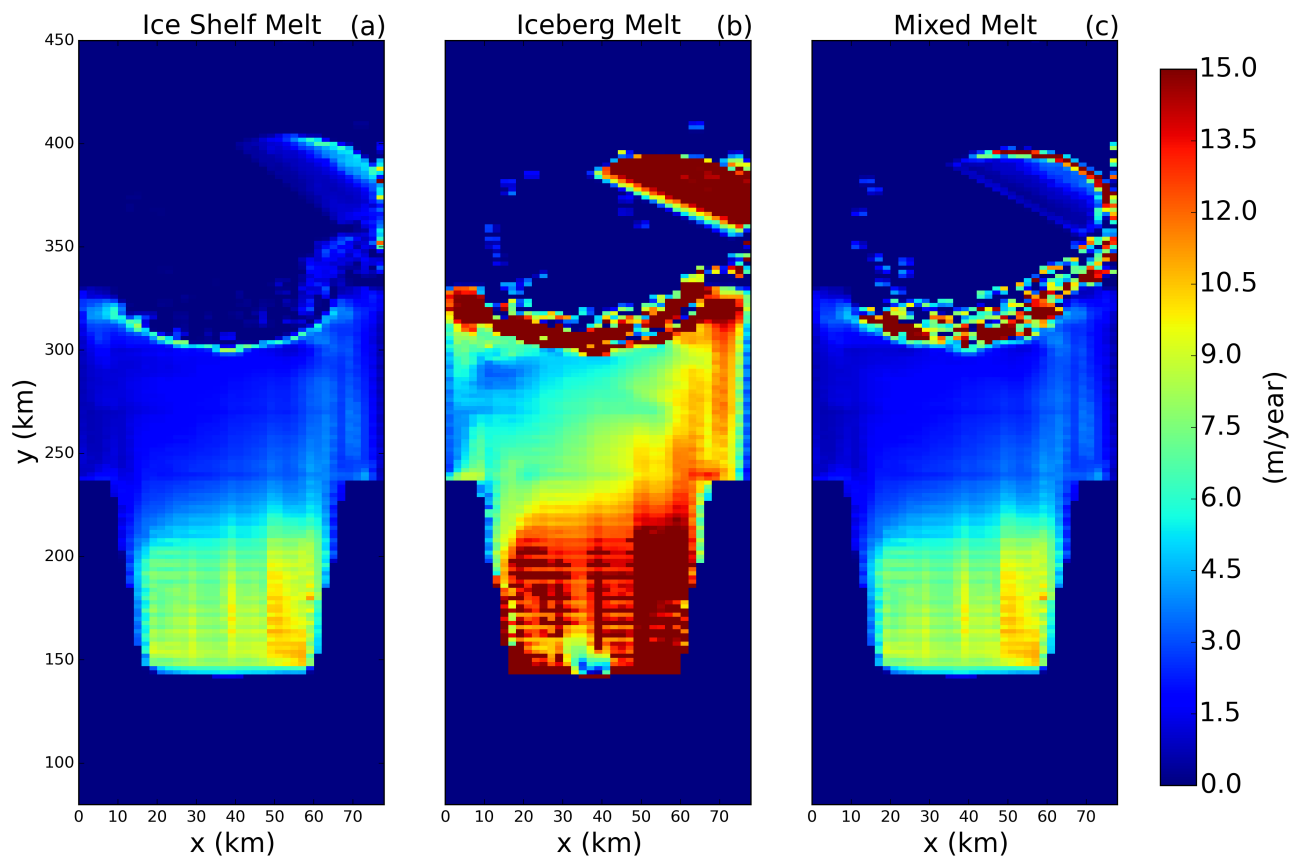


Figure 1. Melt rate 30 days after calving for simulations using melt rates derived using (a) three equation model, (b) icebergs drift parametrization, (c) a mixture between the two (as described in Section 2.5.)